The role of residence time distribution in the continuous steady-state MSMPR crystallization of glycine

Iyke I. Onyemelukwe[a,*], Anna R. Parsons[c], Helen P. Wheatcroft[c], Amy Robertson[c], Zoltan K. Nagy[a,b], Chris D. Rielly[a,*]

[a]*EPSRC Centre for Innovative Manufacturing in Continuous Manufacturing and Crystallization, c/o Department of Chemical Engineering, Loughborough University, Loughborough, Leicestershire, LE11 3TU, UK*
[b]*School of Chemical Engineering, Purdue University, West Lafayette, IN 47907, USA*
[c]*PT&D, AstraZeneca Macclesfield, Silk Road Business Park, Charter Way, Hurdsfield Industrial Estate, Macclesfield, SK10 2NA, UK*

In this work, a vacuum-driven intermittent transfer technique has been implemented to solve transfer line blockage issues and facilitate steady-state cooling crystallization studies of α-glycine in a single- and 2-stage MSMPR crystallizer. Experimental residence time distribution (RTD) analysis of the stirred tank MSMPR cascade is performed using an imperfect pulse method of the axial dispersion model to benchmark the mixing performance against that of tubular crystallizers and determine the influence of RTD on steady-state size distribution of α-glycine product. Process analytical technology (PAT) is used to monitor and understand crystallization process dynamics, and the effect of MSMPR operating temperature, mean residence time, and number of MSMPR stages on mean particle size, crystal size distribution, and yield is studied. Results show the significance of nucleation and growth mechanisms alongside RTD in determining steady-state size distribution, and the need for optimum control of supersaturation to benefit from improved RTDs provided by multistage MSMPR crystallizers.

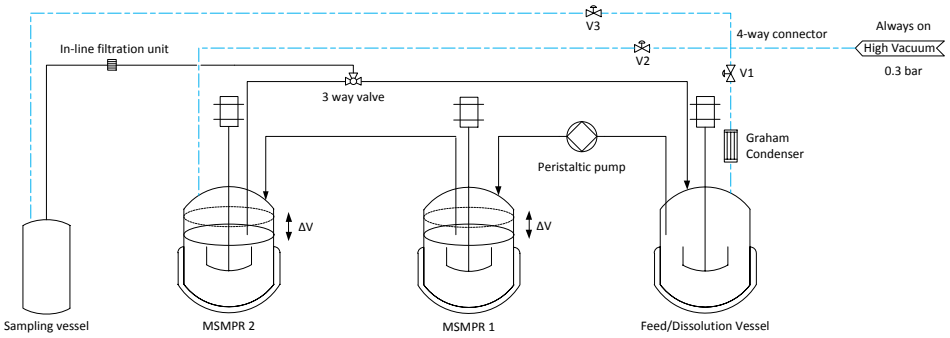

*Iyke I. Onyemelukwe
EPSRC Centre for Innovative Manufacturing in Continuous Manufacturing and Crystallization, Department of Chemical Engineering, Loughborough University, Loughborough, Leicestershire, LE11 3TU, UK
Phone: +44 (0) 7453 322180
Email: I.I.Onyemelukwe@lboro.ac.uk

*Chris D. Rielly
Dean, School of Aeronautical, Automotive, Chemical and Materials Engineering
Department of Chemical Engineering
Loughborough University, Loughborough, Leicester, LE11 3TU, UK
Tel.: +44 (0) 1509 222504
Email: C.D.Rielly@lboro.ac.uk

The role of residence time distribution in the continuous steady-state MSMPR crystallization of glycine

Iyke I. Onyemelukwe[a,†], Anna R. Parsons[c], Helen P. Wheatcroft[c], Amy Robertson[c], Zoltan K. Nagy[a,b], Chris D. Rielly[a,†]

[a]*EPSRC Centre for Innovative Manufacturing in Continuous Manufacturing and Crystallization, c/o Department of Chemical Engineering, Loughborough University, Loughborough, Leicestershire, LE11 3TU, UK*

[b]*School of Chemical Engineering, Purdue University, West Lafayette, IN 47907, USA*

[c]*PT&D, AstraZeneca Macclesfield, Silk Road Business Park, Charter Way, Hurdsfield Industrial Estate, Macclesfield, SK10 2NA, UK*

[†]*Email: I.I.Onyemelukwe@lboro.ac.uk; C.D.Rielly@lboro.ac.uk*

Abstract

In this work, a vacuum-driven intermittent transfer technique has been implemented to solve transfer line blockage issues and facilitate steady-state cooling crystallization studies of α-glycine in a single- and 2-stage MSMPR crystallizer. Experimental residence time distribution (RTD) analysis of the stirred tank MSMPR cascade is performed using an imperfect pulse method of the axial dispersion model to benchmark the mixing performance against that of tubular crystallizers and determine the influence of RTD on steady-state size distribution of α-glycine product. Process analytical technology (PAT) is used to monitor and understand crystallization process dynamics, and the effect of MSMPR operating temperature, mean residence time, and number of MSMPR stages on mean particle size, crystal size distribution, and yield is studied. Results show the significance of nucleation and growth mechanisms alongside RTD in determining steady-state size distribution, and the need for optimum control of supersaturation to benefit from improved RTDs provided by multistage MSMPR crystallizers.

1. Introduction

Continuous crystallization of small molecule active pharmaceutical ingredients (APIs) is currently an area of strong interest in pharmaceutical manufacturing due its potential for delivering consistent particle attributes,[1–3] reducing manufacturing costs through process intensification,[4,5] shortening process development times,[6,7] and providing flexibility in supply.[8] The most common continuous crystallization technologies are the conventional tubular plug flow crystallizer (PFC),[9–12] the tubular continuous oscillatory baffled crystallizer (COBC),[13,14] and the stirred tank MSMPR crystallizer.[15,16] The selection of a suitable crystallization platform is usually guided by system-dependent factors such as crystallization kinetics and fouling/agglomeration propensity,[17] but also the ability of the platform to consistently control a desired critical quality attribute (CQA) while satisfying yield constraints. Additional factors such as solid-liquid density difference, viscosity, and solids loading are important, since they can affect crystallization process performance.[13]

The material residence time distribution (RTD) is an important parameter that describes the time histories of crystals, and as such, the supersaturation histories of all crystals within a continuous crystallizer. Therefore, RTD can affect drug substance CQAs such as the crystal size distribution (CSD), which determines filterability, drying times, and final drug product performance. The control of the full CSD is not possible in practice; however, some of its attributes such as mean size, span, coefficient of variation, and fines fraction can be controlled.[18] A typically large and narrowly distributed crystal product is usually desired from a crystallization process to aid downstream processability.[19] The conventional PFC aims to provide a uniform environment for consistent particles by providing a narrow RTD. This ensures all crystals experience similar histories of supersaturation and hence similar crystal nucleation, growth, and agglomeration rates. The high flow rates required to achieve this, however, means that impractical tube lengths required

for sufficient residence times limit application of the PFC. The COBC overcomes the challenges of the conventional PFC by decoupling mixing from net flow through oscillatory flow. Therefore, longer mean residence times for crystal growth and yield are possible in greatly reduced length to diameter ratios without settling issues. In addition, a range of RTDs is possible by finely controlling the net flow, frequency and amplitude of oscillations. The MSMPR at the opposite end of the mixing spectrum offers an RTD for both solution and crystals that is much broader than usually obtained in tubular crystallizers. The conventional PFC and COBC have been shown to give narrow CSDs[1,9,16,20,21] owing largely to their near-plug flow RTDs, but also tighter control of spatial supersaturation achievable in these platforms. A broad RTD from the backmixed MSMPR therefore suggests that broader CSDs are to be expected in MSMPR crystallization.

Previous works[16,22] have shown that increasing mean residence time in a single-stage MSMPR can improve steady-state CSDs. However, attaining longer mean residence times in an MSMPR usually requires operation at much lower flow rates, which can be a challenge to implement in pump operation due to non-representative withdrawal, and crystal settling during transfer. Su et al.[23] addressed this issue for glycine crystallization using a pump-operated periodic flow MSMPR crystallizer. The technique involved a series of rapid addition and withdrawal cycles and a tuneable holding period between, which allowed the manipulation of material RTD in the MSMPR crystallizer. High flow rates were applied during additions and withdrawals to prevent sedimentation in transfer lines and enable a more representative slurry withdrawal. Interestingly, the periodic flow operation was able to extend mean residence time without overly broadening the material RTD, and larger crystal mean sizes were obtained for the glycine product compared to the continuous flow operation. The periodic flow operation, however, can be described as a hybrid of batch and continuous crystallization, as the MSMPR crystallizer responds to periodic but controlled disturbances

and achieves a "state of controlled operation" rather than the conventional "steady-state" operation described by Randolph and Larson.[15]

Here we investigate the continuous flow crystallization of glycine in an MSMPR crystallizer. Steady-state operation is made possible through the implementation of a vacuum-operated rapid intermittent transfer method,[16] to overcome the limitation of transfer line blockage encountered during pump operation and permit longer mean residence times without compromising continuous operation. This transfer method also ensures isokinetic withdrawal from a well-mixed MSMPR and avoidance of crystal breakage during transfer. Rapid intermittent withdrawal is considered a form of continuous operation since changes in steady-state conditions are negligible when slurry slug size withdrawn is less than 10% of the crystallizer volume.[22,24] Specifically, we study the impact of process parameters including MSMPR temperature and mean residence time on the steady-state product CSD, mean crystal size, and yield. To address the backmixed nature of the MSMPR, different configurations have been employed with the chief aim of obtaining better CSD quality alongside process yield.[25 – 28] Attempts to control product CSD using multistage MSMPR crystallizers have been reported in literature;[29,30] and these studies have suggested that the single-stage MSMPR crystallizer is inefficient, because it produces a product with a broader CSD than the multistage MSMPR crystallizer. Also, in terms of process operability, the single-stage MSMPR crystallizer has limited temperature controllability because of its small heat transfer area.[31] With the inclusion of multiple stages in cascade configuration, RTD can be significantly improved, and the MSMPR system can operate closer to batch equilibrium conditions. For this reason, a 2-stage MSMPR crystallization is also investigated in this work.

Real-time monitoring of crystallization process dynamics, and determination of steady-state operation is achieved by monitoring the particle counts and chord length distribution (CLD) with the aid of an *in situ* focused beam reflectance measurement (FBRM) probe. The counts 1 – 5

μm (#/s) and total counts 1 – 1000 μm (#/s) are related to the total number of crystals in these size bins. The CLD is proportional to the CSD in the crystallizer, and the mean particle size is represented by the square-weighted mean chord length (SWMCL) which is defined as:

$$\text{SWMCL} = \frac{\sum_{i=1}^{k} n_i L_i^3}{\sum_{i=1}^{k} n_i L_i^2} \quad (1)$$

where L_i is the chord length of ith size bin, n_i is the number of counts corresponding to the ith bin, and k is the upper size bin. FBRM has been demonstrated in multiple studies as a sufficient tool for qualitative monitoring of steady-state operation,[27,32 – 34] hence the decision to utilise it here. A characterisation of RTD in the single- and 2-stage MSMPR is performed to assess the role of RTD in controlling glycine steady-state CSD, but also to benchmark the RTD performance of an MSMPR system against tubular crystallizers, since this is seldom visited in literature. Attention is paid to ensuring representative withdrawal by characterising the solids suspension performance of the MSMPR for dense glycine crystals. In addition, the energy constraint on process performance and attainable CSD is practically demonstrated. In all experiments, start-up from equilibrium batch suspension is utilised, with the MSMPR system operated in product recycle mode to minimise material consumption and waste generation.

2. Experimental Section

2.1 Materials

Glycine with ≥99% purity, purchased from Sigma Aldrich UK, was used in preparing feed solution for all experiments. Deionised (DI) water was used as the solvent.

2.2 Experimental setup

Figure 1 and Figure 2 show the schematic of the product recycle single- and 2-stage MSMPR configurations respectively. Two identical 100 ml jacketed glass vessels (model ADAV manufactured by HWS-Labortechnik Mainz) were used as MSMPR 1 and MSMPR 2. Both vessels were unbaffled, had an internal diameter of 60 mm (DN60), and were each fitted with a 3-bladed retreat curve impeller (RCI) of 30 mm diameter. A 500 ml DN100 jacketed glass vessel served as the feed/dissolution vessel. Independent heating and cooling of all vessel jackets was provided by three Julabo recirculating oil baths. The circulating fluid used was Swansil 10 cSt (25 °C) silicone oil with a working range of –40 – 140 °C. Programming of vessel temperature profiles and temperature data logging were achieved via a Labgear software (version 1.2) connected to the oil baths. Rapid intermittent withdrawal was implemented using a high vacuum source controlled via two-way valves (V1, V2, V3) to transfer slurry in the sequence MSMPR 1 → feed/dissolution vessel in the single-stage configuration, and MSMPR 1 → MSMPR 2 → feed/dissolution vessel in the 2-stage configuration. This technique enabled isokinetic withdrawal of suspension in under 2 s from the MSMPR crystallizers.

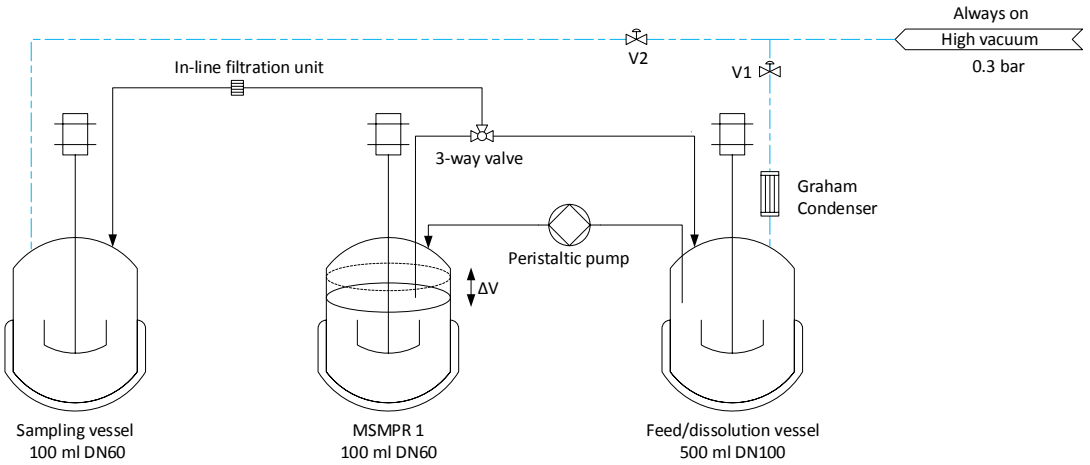

Figure 1 Vacuum connections (dashed) and transfer lines (solid) for the single-stage MSMPR configuration.

A calibrated Masterflex® L/S® peristaltic pump was used to continuously transfer clear feed solution from the feed/dissolution vessel to MSMPR 1 in all experiments. The temperature in the feed/dissolution vessel was maintained at 20 °C above saturation temperature for all experiments, with a condenser attached to minimize solvent loss by evaporation. This ensured fines were absent from the hot feed solution, so that the likelihood of crystal build-up and blockage in the feed line to MSMPR 1 was negligible for the duration of experimental runs. A Mettler Toledo S400 FBRM probe (connected to Mettler Toledo FBRM software version 6.7.0) was placed in MSMPR 1 for the single-stage configuration and moved to MSMPR 2 for the 2-stage MSMPR experiments.

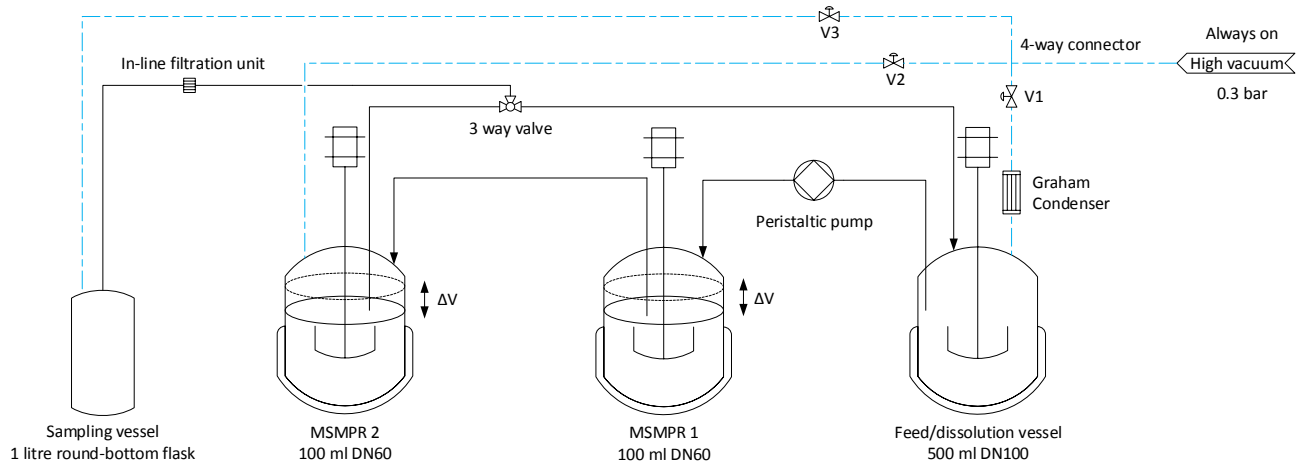

Figure 2 Vacuum connections (dashed) and transfer lines (solid) for the 2-stage MSMPR configuration.

2.3 Liquid RTD characterisation

The effect of volumetric flow rate, mixing intensity (impeller agitation speed), and number of stages on the RTD of the MSMPR system was investigated under continuous steady flow operation. RTD was determined using intrusive pulse tracer measurements, whereby a salt (NaCl) tracer was used, and a pair of conductivity probes (Mettler Toledo InLab® 751-4mm) were positioned as indicated in Figure 3 and Figure 4. This was to enable characterisation by imperfect pulse method which has been shown to be a more accurate way of determining axial dispersion in continuous systems[35] (see section 2.3.1). In all RTD experiments MSMPR 1 and MSMPR 2 were operated at 100 ml of DI water, while the feed/dissolution vessel was operated at 250 ml of DI water (operating below 250 ml was not possible due to impeller clearance limitations).

The RTD performance of a single-stage MSMPR (Figure 3) was determined for different conditions from a test section consisting of MSMPR 1 and MSMPR 2 connected in series by silicone tubing (Masterflex® L/S® platinum-cured) and peristaltic pumps (Masterflex® L/S® Standard Digital Pump). A conductivity probe placed in MSMPR 1 measured the pulse input to

the test section, while a second probe placed in MSMPR 2 measured the output tracer concentration from MSMPR 1 (i.e. the output from MSMPR 1 was sampled at MSMPR 2 for dispersion).

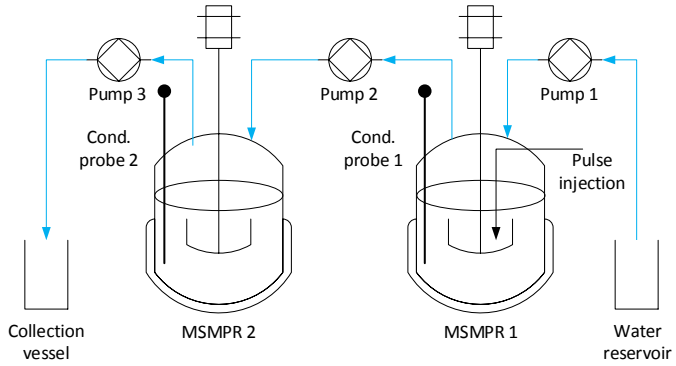

Figure 3 Experimental setup for liquid RTD characterisation of the single-stage MSMPR system.

Subsequently, the RTD of a 2-stage MSMPR system was measured from a test section consisting of the feed/dissolution vessel, MSMPR 1, and MSMPR 2 connected in series according to Figure 4. A conductivity probe was placed in the feed/dissolution vessel to measure the pulse input to the section, and the second conductivity probe in MSMPR 2 measured the tracer exit concentration from MSMPR 1. An interpretation of fitted RTD curves from the measurement points was performed to provide information on the overall extent of axial dispersion in the test section, based on the dimensionless dispersion number, D_{ax}/uL (see section 2.3.1).

At time zero for all experiments, a pulse of 0.5 ml of a 1 M NaCl tracer was injected subsurface close to the impeller in the first vessel in under 1 s using a 1 ml syringe fitted with a flexible capillary tube. Both conductivity probes were started simultaneously via the conductivity meter to record the upstream and downstream response curves (concentration-time curves) at a 1 s interval respectively. Data logging was stopped once readings from both conductivity probes had returned to zero, indicating that the entire tracer had exited the test section. Experiments were

conducted at volumetric flowrates of 25, 50, and 70 ml min^{-1} to vary the mean residence time, τ_L, in the test section (i.e. distance between the measurement points). Impeller speeds were set to 200 and 400 rpm to vary the mixing time in the MSMPR vessels; however, the feed/dissolution vessel could only be operated at 250 rpm due to vortex formation at higher rpm.

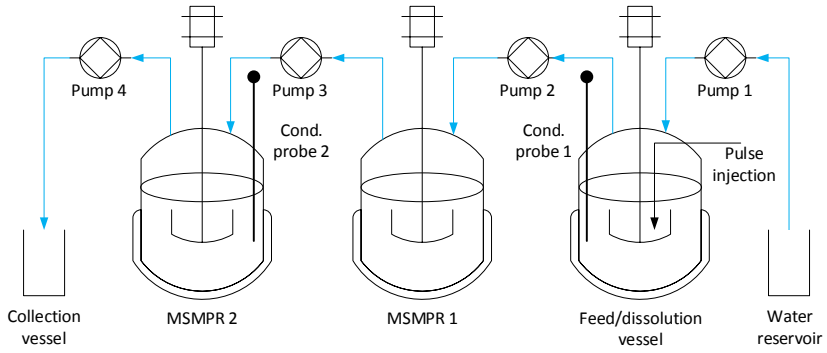

Figure 4 Experimental setup for liquid RTD characterisation of the 2-stage MSMPR system.

The impeller Reynolds number for the MSMPR was calculated using Equation (2):

$$N_{Re} = \frac{\rho_l N D^2}{\mu} \tag{2}$$

where N is the impeller rotation speed (rps), and D is the impeller diameter (m), μ is the bulk fluid viscosity (Pa s), ρ_l is the bulk fluid density (kg m^{-3}).

2.3.1 Determination of axial dispersion from imperfect pulse method

The axial dispersion model describes the mixing behaviour within a test section by superimposing one-dimensional axial dispersion onto convective flow. In the imperfect pulse method of the axial dispersion model,[36] a pair of measurement devices (i.e. conductivity probes in

this case) detect the upstream and downstream concentration-time history of a tracer, since the input tracer pulse may be far from a perfect Dirac delta function[37] which is very difficult to achieve experimentally. For a fixed distance between the upstream and downstream measurement point, the amount of spreading depends on the intensity of dispersion in the system, and this spread can be used to characterise quantitatively the dispersion phenomenon. The imperfect pulse method effectively convolutes the input function from the upstream probe with an axial dispersion model and fits the response to the downstream output function by adjusting the model parameters. The benefit of this method is that the input signal initial shape is arbitrary. In this analysis it is assumed that the axial dispersion model may be applied to any section of a flow to estimate the local liquid dispersion coefficient. The estimates of the degree of backmixing are so described by the dimensionless axial dispersion number, D_{ax}/uL, and a convective time scale:

$$\tau_L = L/u \tag{3}$$

where L is the fixed distance or length of tubing between the measuring conductivity probes (m) in this case, and u is the mean axial velocity (m s^{-1}). The dispersion number characterises axial dispersion as the liquid circulates once through the section in terms of an effective dispersion coefficient, D_{ax} (m^2 s^{-1}). If the dispersion number approaches zero, the region's mixing behaviour is close to plug flow, whereas, for large dispersion numbers, the zone is well-mixed. According to Levenspiel[37], a $D_{ax}/uL > 0.01$ indicates a large deviation from plug flow, while $D_{ax}/uL < 0.01$ indicates a small deviation from plug flow.

The axial dispersion model employed for an *open-open* boundary condition is given in Equation (4)[38]:

$$C(\theta) = \frac{1}{\sqrt{4\pi(D_{ax}/uL)}} exp\left[-\frac{(1-\theta)^2}{4\theta(D_{ax}/uL)}\right] \quad (4)$$

where $C = \frac{(c-c_i)}{\int_0^\infty (c-c_i)dt}$ = dimensionless concentration for tracer (5)

$$\theta = \frac{t}{\tau_L} = \text{dimensionless time} \quad (6)$$

For a linear system, the output response, $C_1(\theta)$, can be determined from the convolution integral of the inlet, $C_0(\theta)$, and the system transfer function, $M(\theta)$:

$$C_1(\theta) = \int_0^\infty M(\theta) C_0^*(\theta - \theta')d\theta \quad (7)$$

Using $M(\theta)$, an output signal can be predicted for any arbitrary continuous input signal. $M(\theta)$ is the response to a Dirac pulse, and is given by Equation (4). The results of the convolution integral can then be fitted to the measured output concentration time history, by adjusting the two model parameters τ_L and D_{ax}/uL. Once the best-fit parameters have been found, D_{ax} may be calculated using Equation (8) and Equation (9):

$$u = \frac{L}{\tau_L} \quad (8)$$

$$D_{ax} = \left(\frac{D_{ax}}{uL}\right)\frac{L^2}{\tau_L} \quad (9)$$

The number of tanks-in-series, n, that best fits the RTD data was calculated from D_{ax}/uL using Equation (10)[39]:

$$n = {uL}/{2D_{ax}} + 1 \quad (10)$$

The tanks-in-series model describes the test section as a series of n equal-sized tanks, thus assuming all tank volumes are identical, and therefore space times are identical.

2.3.2 Parameter estimation method

A series of MATLAB® scripts were written to determine automatically the model parameter giving the best fit between the measured and modelled output signals. An unconstrained optimization function *fminunc* was used to perform the fitting of the two model parameters with bounds for the parameter searching and starting guesses based on the space time between the measurement points. The estimation of the model parameters was carried out by convoluting in the frequency domain and fitting in the time domain.[40,41] After the tracer input signal had been normalized to give $C_0(\theta)$, its Fourier transform was calculated using the fast Fourier transform (FFT) method which is a form of discrete Fourier transform (DFT). The model output concentration was then obtained by multiplying, in the frequency domain, the model transfer function and the experimental input concentration.

2.4 Estimation of just-suspended speed for solids suspension

The just-suspended speed, N_{js}, is the impeller speed at which particles are completely suspended, and no particles remain stationary at the bottom of the vessel for more than 1 – 2

seconds.[42] Complete suspension of solids is important for crystallization as it ensures the maximum crystal surface area is presented to the bulk solution for mass transfer and crystal growth.[43,44] Operating at N_{js} provides near optimal mass transfer between solid and liquid phases; above this speed little mass transfer enhancement is gained despite much higher energy input.[45,46] Ensuring all particles are suspended is a first step towards achieving uniform solids distribution throughout the crystallizer and avoiding size classification through isokinetic slurry withdrawal. This is important because the idealised MSMPR assumes well-mixed contents, which undergo representative withdrawal. In practice, while it is relatively straightforward to achieve homogeneity of the liquid phase, it is usually difficult to suspend the solid phase homogeneously at economic power inputs.[47] The quality of suspension generally increases with impeller speed, and sufficient mixing is necessary to ensure that crystals as much as possible experience similar hydrodynamics and RTD with the bulk solution i.e. no settling or accumulation of solids.

To facilitate rapid process development, N_{js} was estimated using the Dynochem® solid-liquid mixing utility (Scale-up Systems Ltd.), which is a process development and modelling tool for evaluating vessel mixing performance and scale-up. Results of the estimation were confirmed by visual observation at the start of crystallization experiments. Determining N_{js} involved selecting the appropriate vessel and impeller geometry from the utility database and specifying the solid-liquid properties and solids concentration. Based on this information, the utility estimated the impeller speed required for complete suspension of solid particles in the MSMPR. The Dynochem® solid-liquid mixing utility calculates N_{js} based on Zwietering's correlation for solids suspension in stirred tanks[42]:

$$N_{js} = S\nu^{0.1}\left(\frac{g(\rho_p-\rho_l)}{\rho_l}\right)^{0.45} \mathrm{X}^{0.13} d_p^{0.2} D^{-0.85} \qquad (11)$$

where S is the impeller geometrical constant dependent on impeller type, diameter, and clearance, ν is the liquid kinematic viscosity (m^2 s), g is the acceleration due to gravity (m s^{-2}), ρ_p is the particle density (kg m^{-3}), X is the mass ratio of solid to liquid, d_p is the diameter of spherical particles (m), and D is the impeller diameter (m). While the Zwietering correlation has been tested for a wide range of impeller types and solid-liquid properties in vessels of differing scales,[48] it is known to have a number of limitations which can affect the accuracy of its predictions.[43,49,50] A mean particle size of 100 μm was specified for the calculations, as this was the approximate mean size of crystals in the equilibrated start-up batch suspension. The total GLY mass added to the MSMPR for the preparation of the equilibrium batch suspension (saturated at 40 °C) was taken to calculate a weight fraction, X, of 24.8%.

2.5 Critical mean residence time for heat transfer

The critical mean residence time, $\tau_{critical}$, is the minimum time required to cool an incoming feed stream to the desired operating temperature of the MSMPR crystallizer and indicates the cooling capacity of the crystallizer. When operating at a mean residence time, $\tau < \tau_{critical}$, the MSMPR crystallizer may attain a steady-state at undesired supersaturation levels, resulting in unexpected product specification; and the time to attain steady-state may be prolonged. The critical mean residence time for both MSMPR crystallizers was determined using Equation (12) below:

$$\tau_{critical} = \frac{V_{cr}\rho_s C_p (T_f - T_j)}{UA(T_{cr} - T_j)} \quad (12)$$

where V_{cr} is the crystallizer operating volume, ρ_s is the solution density, C_p is the specific heat capacity of the solution at the incoming feed temperature, T_f is the feed temperature, T_j is the MSMPR jacket temperature, T_{cr} is the desired operating temperature of the MSMPR.

2.6 Single-stage MSMPR crystallization

Prior to start-up, 260 ml of a 0.275 g/g solution (saturated at 40 °C) was held at 60 °C in the feed/dissolution vessel. In MSMPR 1, 90 ml of a 0.275 g/g suspension was heated to 50 °C (10 °C above saturation temperature) and held for 30 min to ensure complete dissolution as indicated by FBRM total counts. The clear solution was cooled to an operating temperature of 20 °C to create a batch suspension, and the impeller speed was set to the required rpm to meet hydrodynamic suspension conditions (see section 3.2). Once the batch suspension had equilibrated and FBRM total counts were steady, a start-up sequence was initiated. At start-up, hot feed solution (at 60 °C) was continuously pumped into MSMPR 1 until 10 ml of solution was transferred, filling it to a volume of 100 ml. Immediately, an intermittent withdrawal of slurry from MSMPR 1 was initiated through a vacuum operation in which ~10% of the crystallizer volume was transferred via a dip pipe to the feed/dissolution vessel every 1/10th of τ. The average working volume in MSMPR 1 and the feed/dissolution vessel was 90 ml and 250 ml respectively, with ~10 ml transferred between both vessels. On attainment of steady-state, a sample was isolated by means of an integrated sampling and filtration arrangement which rapidly separated product crystals from mother liquor. The CSD of the product crystals was measured in a Malvern Mastersizer® 2000 using a wet dispersion unit with isopropanol as dispersant. The final steady-state concentration of the mother liquor was determined gravimetrically, and the process yield was calculated for each

experiment as the amount of product obtained from the crystallizer relative to the amount of available supersaturation using Equation (13):

$$Yield = \frac{C_f - C_{ss}^i}{C_f - C^*} \times 100 \quad (13)$$

where C_f is the feed concentration to MSMPR 1, C^* is the equilibrium concentration at the specified operating temperature, and C_{ss}^i is the steady-state concentration in the ith crystallizer. The supersaturation is defined as C_{ss}^i / C^*. Steady-state operation was attained when the total counts and SWMCL showed no significant increasing or decreasing trend. This signified that the rate of generation of crystal mass due to secondary nucleation and/or attrition equalled the removal rate of crystals from the MSMPR crystallizer.

2.7 2-stage MSMPR crystallization

For the cascade study, feed solution and batch suspension preparation were similar to those employed in the single-stage MSMPR crystallization. Each MSMPR crystallizer contained a 90 ml suspension of 0.275 g/g (saturated at 40 °C) which was heated to 50 °C and held for 30 min for complete dissolution. The clear solutions in MSMPR 1 and 2 were cooled to 20 °C and 10 °C respectively to create the starting batch suspensions. The impeller speed in each MSMPR crystallizer was set to the required rpm for effective mixing, and real-time monitoring of the crystallization process was via an FBRM probe positioned in MSMPR 2. At steady-state operation, samples were taken from both MSMPR stages for final concentration determination, CSD analysis, and microscope imaging.

3. Results and discussion

3.1 Liquid RTD characterisation

Figure 5 shows the normalized input and output response curves (C-curves) for an experiment performed at a flow rate of 70 ml min^{-1} and 400 rpm. The tracer input to MSMPR 2 was taken as the output concentration from MSMPR 1 (red curve) according to Figure 3. This represents the RTD of material going into the next stage. Figure 5 shows a good fit with experimental data using the transfer function of the imperfect method. The green curve is the model predicted response fitted to the output response from MSMPR 1 to determine the number of equal-sized tanks, n, that give approximately the same RTD as the test section considered. In this case, n was determined as 1.4.

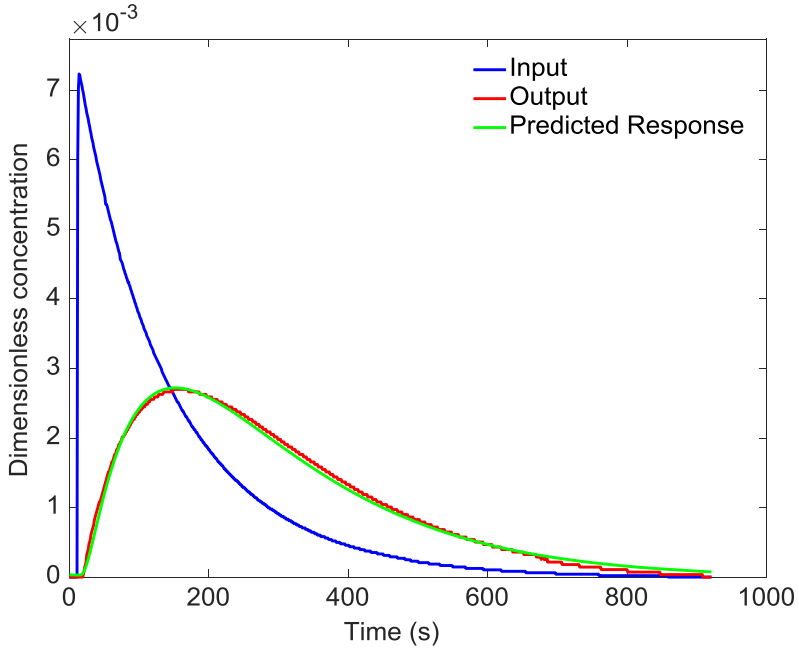

Figure 5 Normalized input and output curves for the single-stage MSMPR configuration with dispersion model fitting for imperfect pulse method. Volumetric flow rate of 70 ml min^{-1} and agitation speed of 400 rpm. $n = 1.4$.

Figure 6 shows the different pulse input shapes and corresponding output curves measured at different flow rates for an impeller speed of 200 rpm. From the analysis of these experimental C-curves and corresponding D_{ax}/uL values in Figure 7, it was concluded that increasing impeller speed beyond 200 rpm had negligible effect on RTD performance. This suggests that short mixing times are already achieved at 200 rpm, whereby the salt tracer is quickly mixed with the bulk liquid in the MSMPR. This is observable from the input curves in Figure 5 and Figure 6 where a rapid rise in tracer concentration is followed by a gradual decay expected of a continuous stirred tank. Previous work by Choi et al.[51] and Patwardhan[52] has shown that vessel RTD performance increases with increasing impeller speed from 0 rpm until a constant value at ~100 rpm. Effective mixing is essential in the MSMPR to ensure that incoming feed solution is well-mixed with vessel contents for uniform distribution of temperature and supersaturation throughout the vessel volume.

Increasing volumetric flow rate was found to have little effect on the RTD performance of a single-stage MSMPR. For flow rates of 25, 50, and 70 ml min^{-1} ($\tau = 4$, 2, and 1.4 min respectively), D_{ax}/uL was in the range 0.86 – 1.24 ($n = 1.59 – 1.48$). Choi et al.[51] showed that similar RTDs were obtained in an unbaffled 1.4-litre stirred tank regardless of volumetric flowrate; thus, confirming impeller speed as the controlling parameter for vessel RTD performance. This implies that changing the mean residence time in an MSMPR would cause no significant change to the RTD of vessel contents. This outcome supports simulation results obtained by Su et al. (2017) for a continuously operated 500 ml MSMPR crystallizer, whereby doubling the mean residence time did not significantly change the RTD coefficient of variation (c.v. $= \sigma/\tau$). For the single-stage MSMPR system, D_{ax}/uL was determined as 1.07 $\pm$ 0.13, with n of 1.5 $\pm$ 0.05.

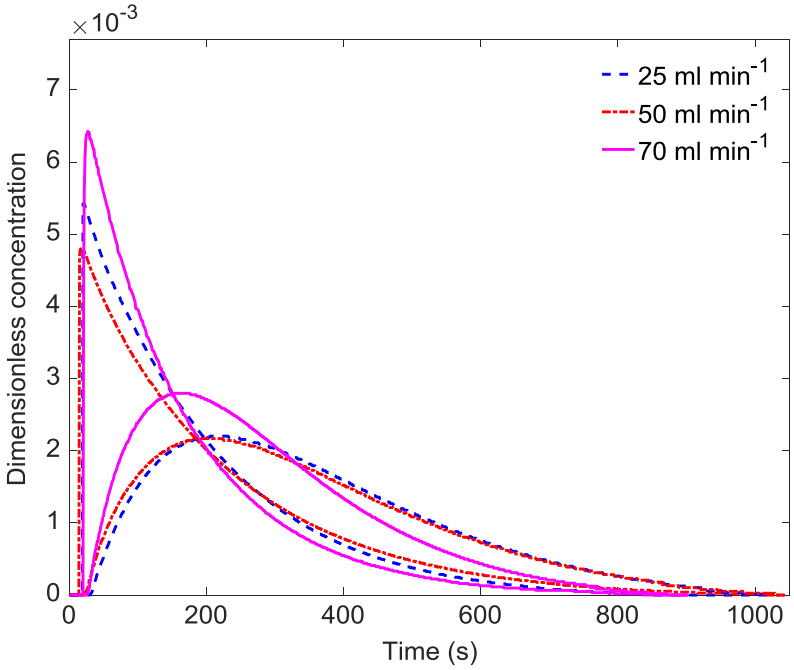

Figure 6 Normalized input and output curves measured for the single-stage MSMPR configuration at 200 rpm.

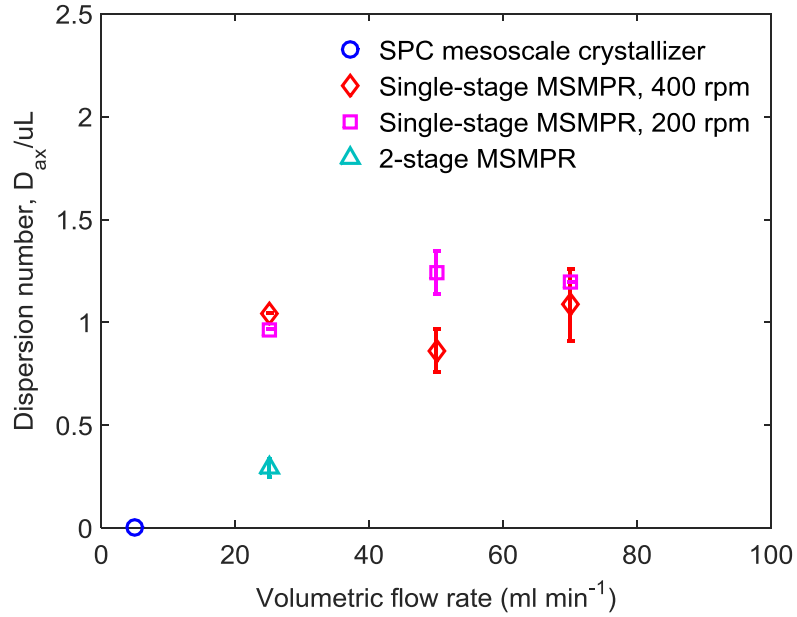

Figure 7 Effect of volumetric flow rate and impeller speed on RTD performance of the MSMPR system.

Adding a second stage significantly improved RTD performance by lowering D_{ax}/uL to 0.292 ± 0.04, with a corresponding n of 2.75 due to the feed/dissolution vessel operating at a higher volume of 250 ml. The improved RTD of the 2-stage MSMPR is still far off from the performance of a tubular COBC such as the SPC mesoscale crystallizer[35,53] (see Table 1) which easily approximates to plug flow ($D_{ax}/uL = 0.002$; $n = 251$) at optimal oscillatory conditions and much lower mixing intensity, regardless of volumetric flow rate. This highlights the intrinsically broad RTDs of MSMPRs, indicating that broader product CSDs are to be expected from MSMPR crystallizers in comparison to tubular crystallizers. The outcome of the RTD study suggests that crystallizations performed in the single-stage MSMPR crystallizer at different mean residence times should essentially have the same material residence time distributions. Results also signify that operating in a 2-stage MSMPR system could potentially decrease CSD span compared to a single-stage MSMPR crystallizer, while increasing total mean residence time for improved yield.

Table 1 Comparison of axial dispersion performance between the MSMPR crystallizer and SPC mesoscale crystallizer

Crystallizer	Stages/ length (m)	Flow rate (ml min^{-1})	Mixing intensity, N_{Re}/Re_o	τ_L (sec)	D_{ax}/uL (-)	D_{ax} (m^2 s^{-1})	Calculated tanks, n (-)
MSMPR	1	25	3364	40.1	0.966	8.5×10^{-3}	1.52
	1	25	6728	74.4	1.044	4.7×10^{-3}	1.48
	1	50	3364	22.7	1.243	1.7×10^{-2}	1.48
	1	50	6728	29.7	0.863	1.2×10^{-2}	1.59
	1	70	3364	23.2	1.197	1.6×10^{-2}	1.42
	1	70	6728	20.5	1.086	1.8×10^{-2}	1.47
	2	25	6728	193.3	0.292	1.1×10^{-3}	2.75
SPC mesoscale	9	5	371	-	2.0×10^{-3}	6.3×10^{-5}	251

3.2 Just-suspended speed

With RTD performance of the MSMPR configurations now understood, good solid-liquid mixing in the MSMPR is necessary to ensure crystals experience similar RTD with the bulk solution. For the conditions specified in Table 2, N_{js} was computed as 554 rpm ± 20%. This

corresponded to a total specific power input of 0.079 W kg^{-1}, and a vessel Reynolds number of 8310. A visual inspection of the start-up suspension found that an impeller speed of 500 rpm was sufficient for complete suspension of particles, and the suspension in the crystallizer appeared uniform (i.e. no axial settling or suspension gradients). The impeller speed was therefore maintained at this condition to minimise crystal attrition during crystallization. To check for representative withdrawal at steady-state, the CSD of a sample obtained via intermittent withdrawal was compared with a sample taken from the bottom of MSMPR 2 at the end of the 2-stage MSMPR crystallization. The results are discussed in section 3.5.

Table 2 Specified conditions for calculating just-suspended speed, N_{js}

	Specification	Values
Vessel geometry	Base shape	DIN Torispherical
	Inner diameter (mm)	60
	Total height to tan (mm)	55
Impeller	Impeller type	3-bladed retreat curve impeller
	Tip diameter (mm)	30
	Clearance from base (mm)	10
	Impeller S number (-)	3.5
Mixing duty	Liquid volume (l)	0.1
	Liquid fill height (mm)	39
	Mass of solids (kg)	0.025‡
	Mass ratio of solid to liquid, X (%)	24.78
Physical properties	Liquid density, ρ_l (kg m^{-3})	1000
	Liquid dynamic viscosity (cP)	1.0
	Particle density, ρ_p (kg m^{-3})	1610
	Mean particle size (μm)	100
Performance at N_{js}	Specific power input (W kg^{-1})	0.079
	Vessel Reynolds number (-)	8310
	Tip speed (m s^{-1})	0.87

‡Solids mass based on GLY solution concentration at 40 °C.

3.3 Critical mean residence time

AspenONE® engineering suite was used in estimating C_p as 3823 J kg^{-1} K^{-1} for the GLY-water solution with density of 1090 kg m^{-3} and the UA for MSMPR 1 and 2 was estimated at 2.39

W K^{-1} using the Dynochem® UA utility. The critical mean residence time, $\tau_{critical}$, was calculated as 9.06 min for a desired operating temperature of 20 °C and an incoming feed temperature of 60 °C, with the MSMPR jacket temperature set to 0 °C. Table 3 summarises the specifications and results.

Table 3 Specified conditions for estimating UA

	Specification	Values
Vessel geometry	Liquid volume (l)	0.1
	Heat transfer area, A (m^2)	0.01
Process side	Impeller speed (rpm)	500
	Process heat transfer coefficient, h_i (W m^{-2} K^{-1})	3557
	Overall heat transfer coefficient, U (W m^{-2} K^{-1})	239
Wall and lining	Wall thickness (mm)	2.5
	Wall thermal conductivity (W m^{-1} K^{-1})	1.09
	Material of construction	Borosilicate
	Wall heat transfer coefficient, h_w (W m^{-2} K^{-1})	301
Jacket side	Heat transfer medium	SYLTHERM 8002
	Jacket type	Annular unbaffled
	Jacket heat transfer coefficient, h_o	1739

3.4 Single-stage MSMPR crystallization

Table 4 summarises the operating conditions and results for Experiment 1 – 5 in the single-stage MSMPR crystallizer. In all experiments performed, α-GLY was consistently produced, as confirmed by offline Raman spectroscopy (Figure 8). Figure 9 shows the process time diagram for Experiment 1 which was operated with a mean residence time of 5 min. From the evolution of the FBRM statistics, four distinct phases were identified in the MSMPR crystallizer. In the start-up phase, MSMPR 1 was cooled to trigger spontaneous nucleation and create an initial batch suspension. Steadily decreasing total counts 1 – 1000 µm and counts 1 – 5 µm indicated a loss of crystal mass during the washout phase. This was driven primarily by the simultaneous withdrawal of start-up suspension and addition of feed solution to the crystallizer. In addition, the rapid addition of hot feed solution elevated the MSMPR temperature by ~10 °C, causing a decrease in

supersaturation and further loss of crystals by dissolution. An accompanying increase in SWMCL indicated a predominantly bigger crystal population in MSMPR 1 from fines dissolution and crystal growth.

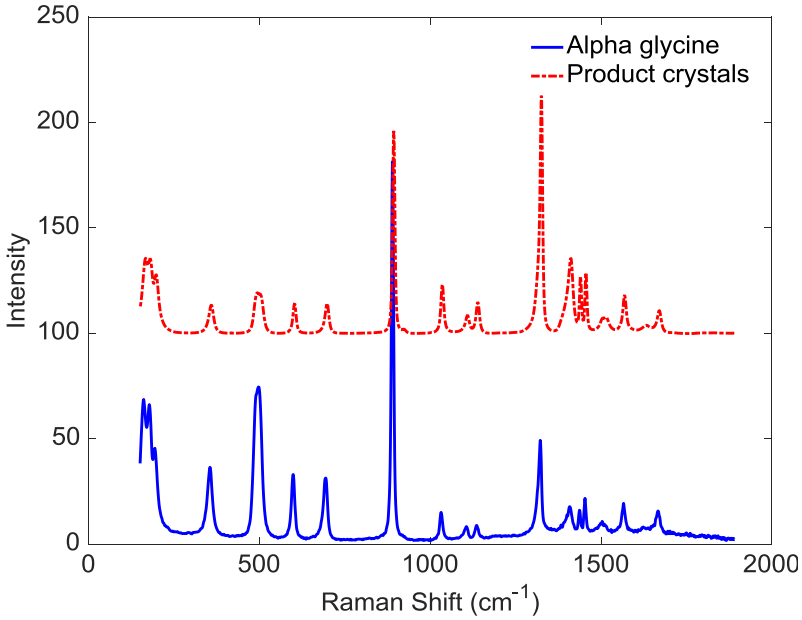

Figure 8 Offline Raman spectra for α-GLY and product crystals obtained.

A response phase was initiated at ~23 min when a low enough MSMPR temperature generated sufficient supersaturation to trigger secondary nucleation. The response phase signified a transition to a secondary nucleation-controlled crystallization, as indicated by rising total counts and a decreasing mean chord length. Generally, the magnitude of a response phase depends on the maximum supersaturation generated in the MSMPR, which is dictated by the feed addition rate, heat removal rate of the MSMPR, and suspension density. In Experiment 1, a short mean residence time of 5 min allowed for rapid build-up of supersaturation, which caused faster nucleation rates and an observable response phase. For longer mean residence times in Experiment 2 and 3, the response phase was much less pronounced.

Table 4 Summary of operating conditions and experimental results for single-stage MSMPR crystallization

	Experiment				
	1	2	3	4	5
Mean residence time, τ (min)	5	10	15	20	10
Feed/dissolution vessel temperature (°C)	60	60	60	60	60
MSMPR 1 operating temperature (°C)	27	20	20	20	10
Pump flow rate (ml min^{-1})	20	10	9.33	5	10
Avg. operating volume (ml)	90	90	90	90	90
Residence times to steady-state (-)	5	3.2	5	n/a	n/a
Feed concentration, C_f (g/g)	0.275	0.275	0.275	0.275	0.275
Exit from MSMPR 1, C_{ss}^1 (g/g)	0.2543	0.2225	0.2146	n/a	n/a
MSMPR 1 supersaturation (-)	1.206	1.234	1.190	n/a	n/a
Steady-state FBRM total counts (#/s)	2,741	3,334	1,645	n/a	n/a
Steady-state mean crystal size, $d_{4,3}$ (µm)	444	768	833	n/a	n/a
Span (-)	3.33	1.59	1.39	n/a	n/a
Yield (%)	33	56	64	n/a	n/a

Unsurprisingly, MSMPR 1 did not attain the desired operating temperature of 20 °C following the addition of the hot feed solution, and instead the MSMPR temperature oscillated around ~27 °C (see Figure 9), causing fluctuations in local supersaturation. This was a result of the inadequate cooling capacity of the MSMPR for operation below $\tau_{critical}$ as earlier determined in section 3.3. Temperature profiles in Figure 10 demonstrate the inability of MSMPR 1 to achieve the setpoint even at a minimum jacket temperature of –4.5 °C. The oil bath was unable to cool beyond this temperature, and subsequently entered cooling and heating cycles. For a mean residence time of 5 min, attaining the desired operating temperature would require cooling the jacket to –42 °C, a temperature beyond the working range of silicone oil. The result of a higher MSMPR operating temperature, and insufficient time for crystal growth was a heavily saturated steady-state suspension in MSMPR 1 with a poor yield of 33% (see Table 4).

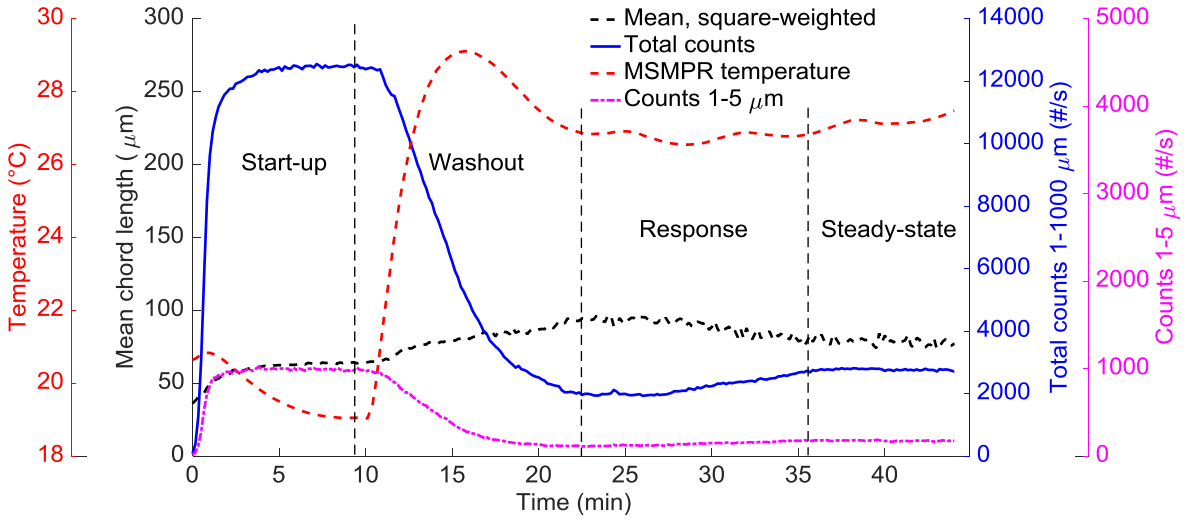

Figure 9 Process time diagram for Experiment 1 in the single-stage MSMPR crystallizer showing temperature, total counts, and square-weighted mean. $\tau = 5$ min.

Experiment 1 highlighted the heat transfer limitation imposed on the degree of supersaturation achievable in MSMPR 1, and therefore, the minimum obtainable product mean size. Previous work by Power et al.[54] has shown the impact of energy balance constraints on minimum particle sizes attainable in MSMPR crystallizers. When compared to tubular crystallizers, stirred tank crystallizers have smaller surface area to volume (SAV) ratios, which essentially is the available heat transfer area per unit volume within the crystallizer. In this instance, MSMPR 1 has an SAV of 100 m^{-1}, which is much smaller than the SAV of the SPC mesoscale crystallizer (1190 m^{-1}).[53] As a result, the excellent heat transfer performance of tubular crystallizers enables the attainment of high degrees of supersaturation during cooling crystallizations for faster nucleation rates. However, challenges with encrustation currently limit the use of primary and secondary nucleation for achieving small crystal mean sizes in these devices.[13,17]

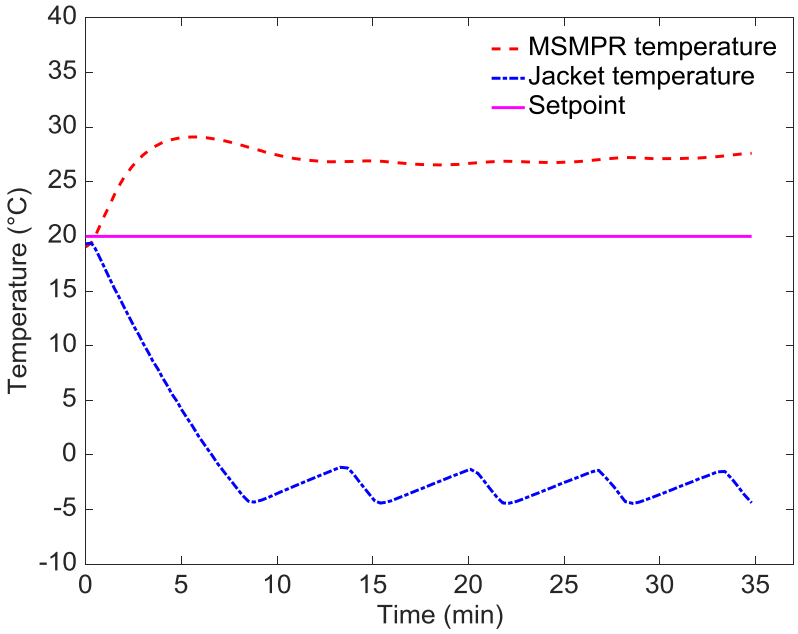

Figure 10 Temperature profile in MSMPR 1 for Experiment 1.

Experiment 2 and 3 (Figure 11 and Figure 12) showed no detectable response phase as total counts 1 – 1000 µm steadily decreased and levelled off into a steady-state. The supersaturation generated by feed addition was consumed mainly by growth of crystals in the initial batch suspension. This was indicated by a steady rise in mean chord length throughout the washout phase. The presence of crystals in the 1 – 5 µm size range indicated that secondary nucleation necessary to sustain crystal mass was occurring on a much smaller magnitude. Both mean residence times ($\tau > \tau_{critical}$) permitted operation of MSMPR 1 at the desired temperature, and promoted crystal growth as indicated by steady-state mean crystal sizes ($d_{4,3}$) obtained (see Table 4). It follows therefore, that increasing mean residence time will lower supersaturation in the MSMPR crystallizer and cause less secondary nucleation than growth to occur; thereby giving rise to bigger crystals, improved yield, and a narrower CSD. It is evident from Figure 13, that as mean residence time was increased, a reduction in the fine end of the steady-state distribution occurred, however no notable change in the coarse end of the CSD was observed. This is because as mean residence

time increases, crystals on average spend more time in the crystallizer, and smaller crystals grow towards larger sizes, in this way a narrowing of the distribution occurs. It was also observed that longer mean residence times in MSMPR 1 produced a lower steady-state crystal population as indicated by total counts 1 – 1000 µm in Table 4. Experiment 1, however, had relatively lower total counts at steady-state than expected, due to operation at a much lower steady-state supersaturation than had been targeted.

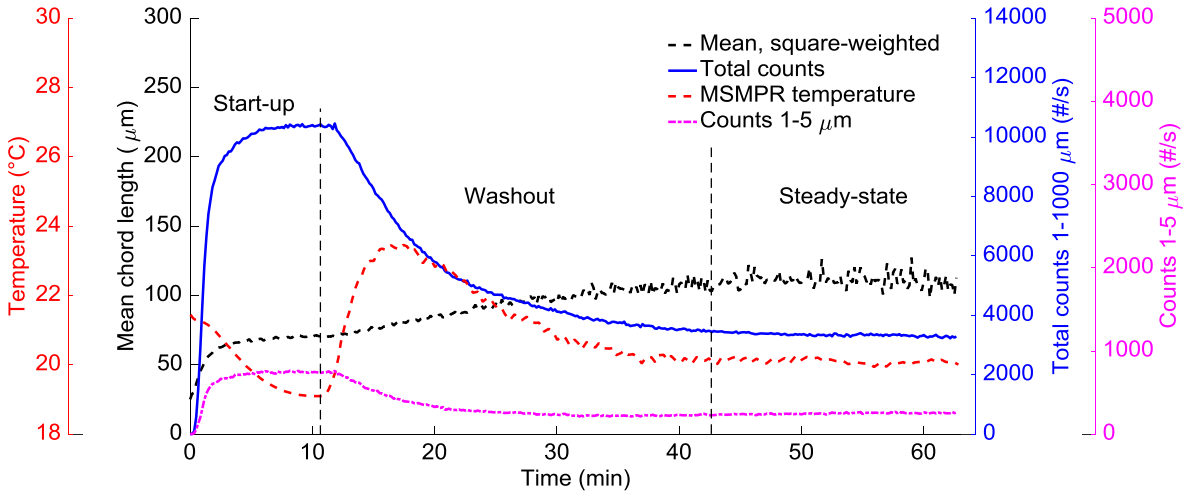

Figure 11 Process time diagram for Experiment 2 in the single-stage MSMPR crystallizer showing temperature, total counts, and square-weighted mean. $\tau = 10$ min.

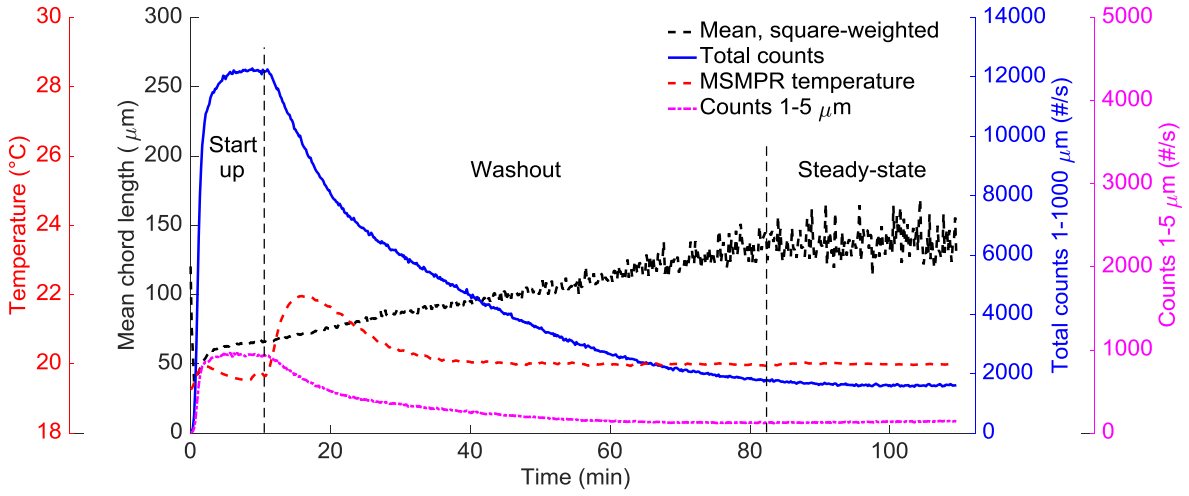

Figure 12 Process time diagram for Experiment 3 in the single-stage MSMPR crystallizer showing temperature, total counts, and square-weighted mean. $\tau = 15$ min.

Despite all three experiments having similar RTDs (for the same MSMPR), the steady-state product CSD from Experiment 1 was very different to Experiment 2 and 3. Strongly competing secondary nucleation in Experiment 1 created excessive fines and a bimodal distribution. The presence of fines and predominantly needle-shaped crystals are clearly visible in offline images of the isolated product (see Figure 14(a)). Doubling the mean residence time in Experiment 2 narrowed the span of the distribution and increased the mean size of the steady-state product. It can be said that Experiment 2 and 3 had similar steady-state CSDs due to weakly competing secondary nucleation in both experiments. The steady-state supersaturation of these two experiments are also not very different as seen in Figure 15. A marginal improvement to the product mean size, CSD span, and yield was however obtained in Experiment 3. Figure 14(b) and Figure 14(c) show the more regular prismatic shape of α-GLY obtained from the growth-dominated processes of Experiment 2 and 3 respectively. Extending the mean residence time to 20 min (Experiment 4) produced enormous crystals (see Figure 14(d)) which clogged the transfer line

between MSMPR 1 and the feed/dissolution vessel. This indicated that larger tubing inner diameters are required for longer mean residence times to cope with fast-growing α-GLY crystals.

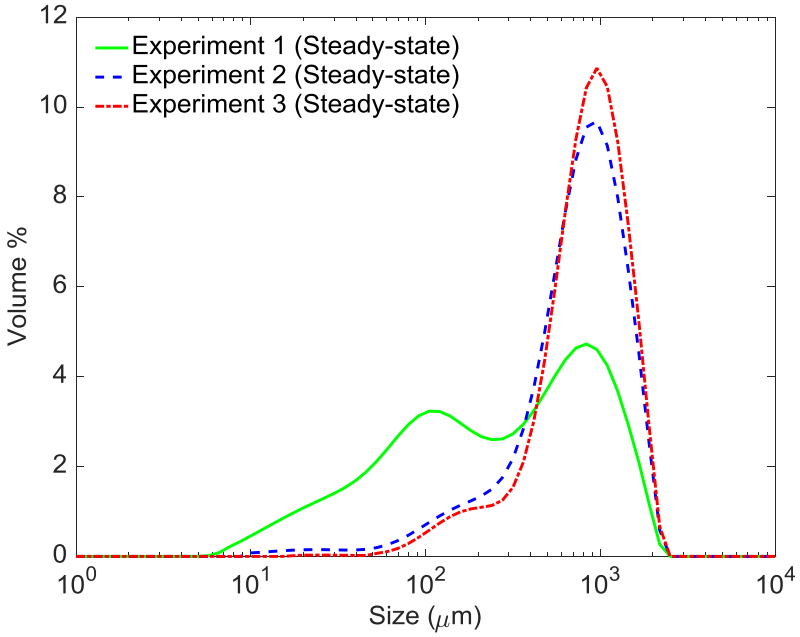

Figure 13 Steady-state α-GLY product CSDs obtained for Experiment 1, 2, and 3.

The results from Experiment 1 – 3 highlight the greater role of crystallization mechanisms than RTD in shaping the final product CSD. The mean residence time does not change RTD, but it controls the rate of supersaturation generation and consumption in the crystallizer, which influences competing mechanisms. Since nucleation and growth rates are determined by available supersaturation, it is important to control supersaturation to promote one mechanism over the other, since the ratio of both mechanisms significantly affects product CSD. Minimising nucleation becomes necessary in this case since it creates substantial fines in the product. For the fast-growing α-GLY, Experiment 2 and 3 therefore suggest that extending the mean residence time in the MSMPR will promote growth over nucleation and give a better-quality product with improved yield.

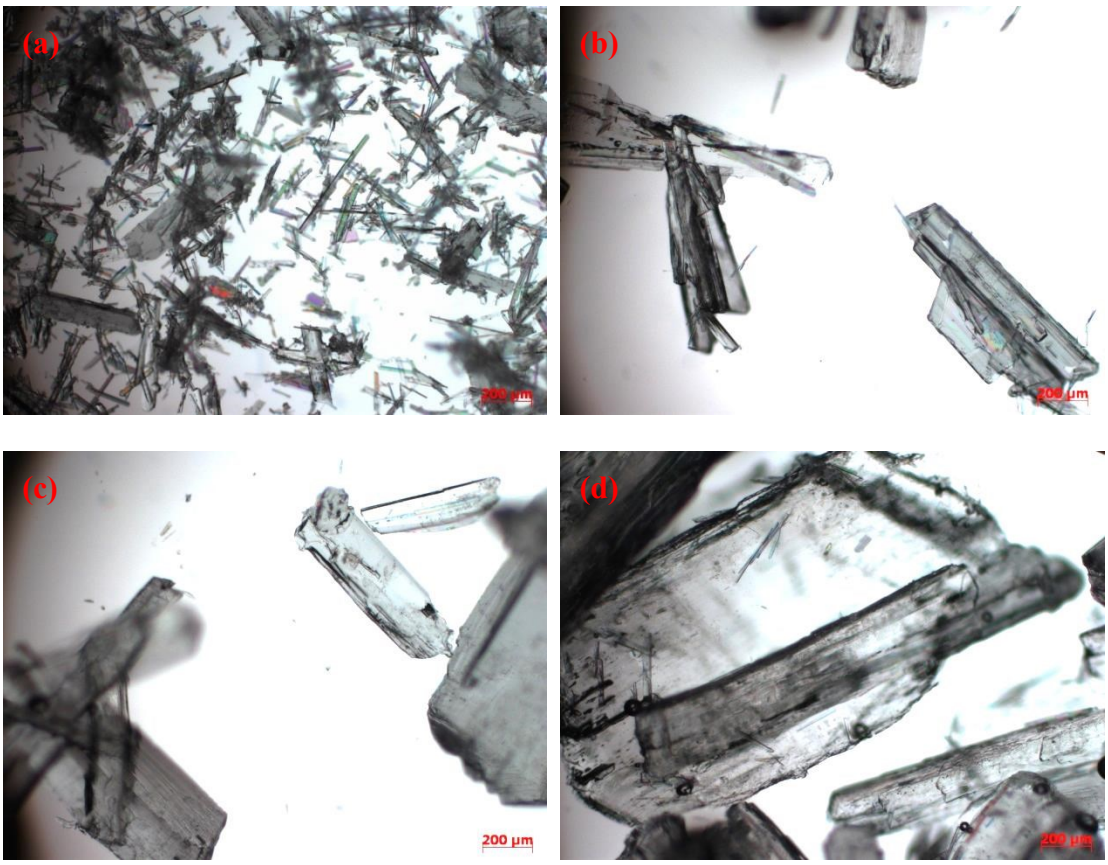

Figure 14 Microscope images of α-GLY product crystals from (a) Experiment 1 (at steady-state); (b) Experiment 2 (at steady-state); (c) Experiment 3 (at steady-state); (d) Experiment 4 (after blockage).

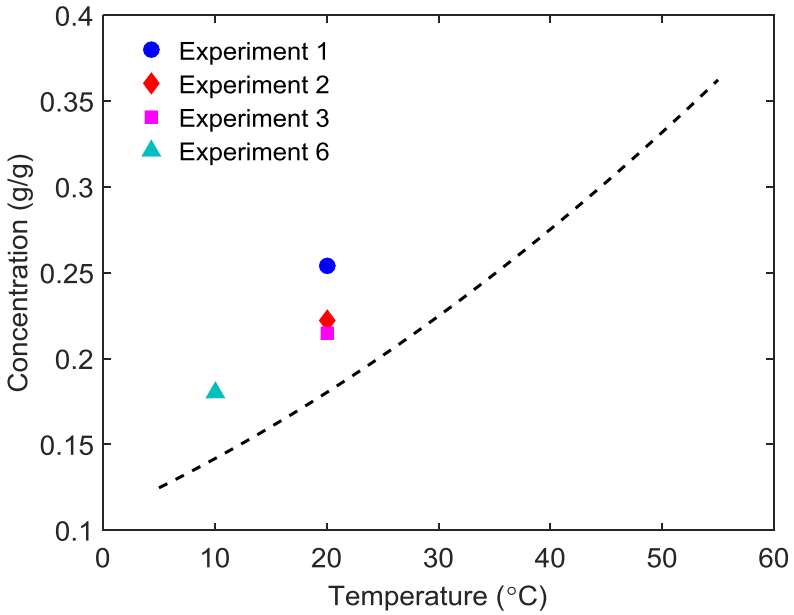

Figure 15 Steady-state concentrations for single-stage and 2-stage MSMPR experiments. Black dashed line is the solubility curve.

The downside of prolonged mean residence times in a single-stage MSMPR is that high throughput times of a batch crystallizer will be approached without achieving the equivalent thermodynamic yield (i.e. recovered solute fraction), since the MSMPR operates at a fixed point (supersaturation) in the phase diagram. To improve thermodynamic yield, operation of the single-stage MSMPR at a lower point in the phase diagram (MSMPR temperature of 10 °C) was attempted. This was however unsuccessful, as a high degree of supersaturation caused significant encrustation on the FBRM probe and crystallizer walls in Experiment 5. Therefore, the 2-stage MSMPR crystallizer was explored.

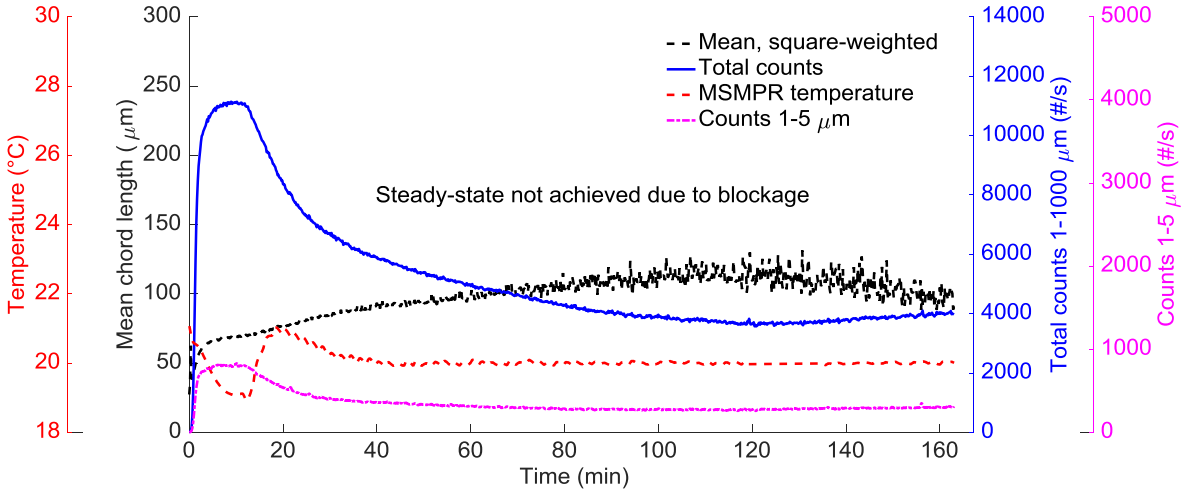

Figure 16 Process time diagram for Experiment 4 in the single-stage MSMPR crystallizer showing temperature, total counts, and square-weighted mean. $\tau = 20$ min.

3.5 2-stage MSMPR crystallization

In Experiment 6, the 2-stage MSMPR crystallizer enabled continuous operation at a lower point in the phase diagram without fouling and encrustation issues encountered in Experiment 5 (see Figure 15). Table 5 summarises the operating conditions and results for Experiment 6. The process time diagram in Figure 17 shows a strong response phase in MSMPR 2 driven by significant supersaturation. Substantial secondary nucleation was evidenced by steadily increasing counts 1 – 5 μm which produced a high crystal number density (total counts) at steady-state. Figure 18 shows that the steady-state CSD from MSMPR 2 had a fraction of smaller crystals created by a secondary nucleation-dominated process. With a high suspension density, crystal-crystal and crystal-impeller collisions are promoted; and as glycine crystals approach larger sizes (~798 μm)[23] the propensity for attrition increases. These combined mechanisms produced a smaller product mean size.

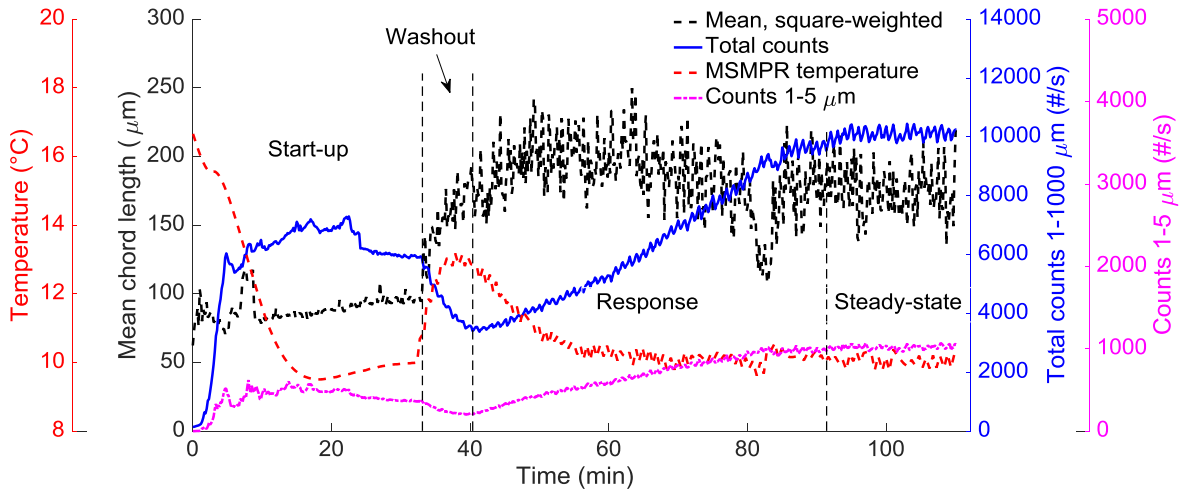

Figure 17 Process time diagram for Experiment 6 in the 2-stage MSMPR system showing MSMPR 2 temperature, total counts, and square-weighted mean. $\tau = 10$ min.

Table 5 Summary of operating conditions and experimental results for 2-stage MSMPR crystallization

	Experiment 6		
	Feed	MSMPR 1	MSMPR 2
Mean residence time, τ (min)	25	10	10
Vessel operating temperature (°C)	60	20	10
Avg. operating volume (ml)	250	90	90
Feed concentration, C_f (g/g)	0.275	n/a	n/a
Exit from MSMPR, C_{ss}^i (g/g)	n/a	n/a	0.180
MSMPR supersaturation (-)	n/a	n/a	1.24
Steady-state FBRM total counts (#/s)	n/a	n/a	10,111
Steady-state mean crystal size, $d_{4,3}$ (µm)	n/a	805	528
Span (-)	n/a	1.58	2.37
Yield (%)	n/a	n/a	71

In contrast, the steady-state CSD from MSMPR 1 had a larger mean size and smaller span, indicating that crystal growth was dominant in the crystallizer. Offline microscope images in Figure 19(a) confirm the absence of significant fines in the isolated product from MSMPR 1.

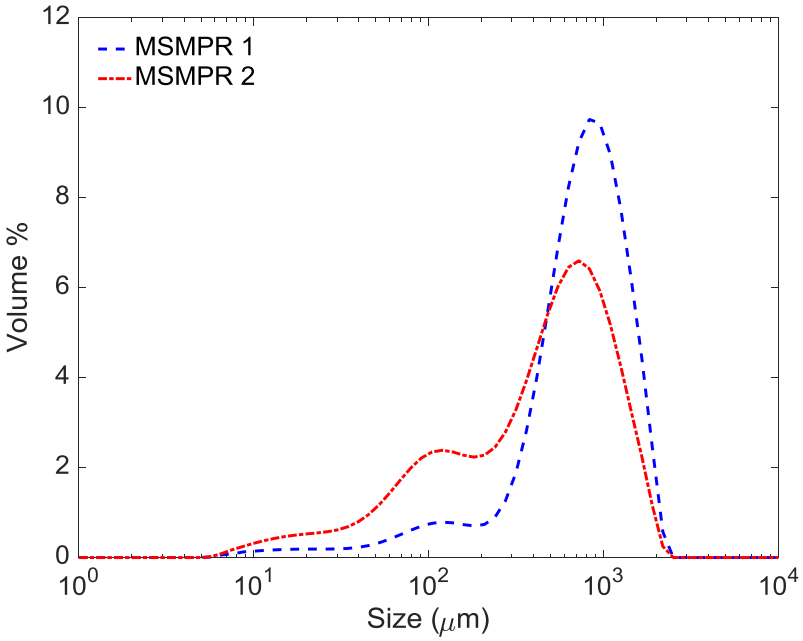

Figure 18 Steady-state α-GLY product CSDs obtained from MSMPR 1 and 2 in Experiment 6.

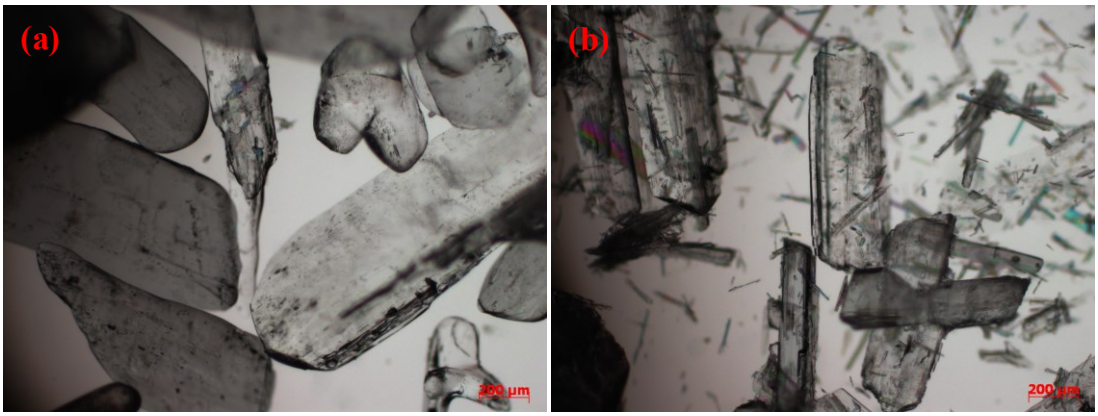

Figure 19 Microscope images of steady-state α-GLY product crystals from MSMPR 1 (a) and MSMPR 2 (b) in Experiment 6.

Figure 20 shows the similarity in steady-state CSDs from the single-stage MSMPR in Experiment 2 and MSMPR 1 in Experiment 6 for the same mean residence time and RTD. Fewer fines in MSMPR 1 suggests less secondary nucleation than in the single-stage MSMPR. This is to be expected for a complete recycle operation, since an added crystallization stage (MSMPR 2) would

further decrease solution concentration in the feed/dissolution vessel, and consequently the supersaturation in MSMPR 1.

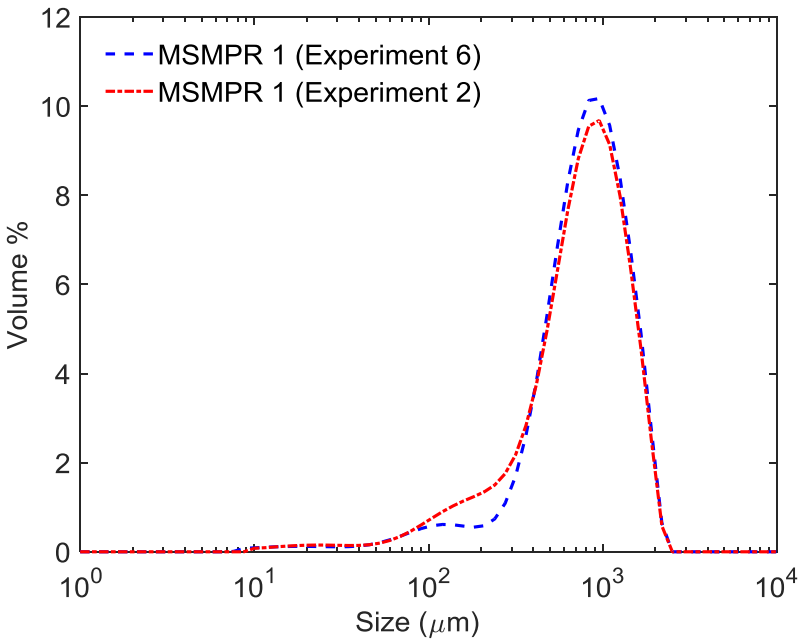

Figure 20 Comparison of steady-state α-GLY product CSDs from the single-stage MSMPR in Experiment 2 and MSMPR 1 in Experiment 6.

The 2-stage cascade achieved a higher thermodynamic yield than could be attained in the single-stage MSMPR system, by overcoming practical limitations. However, despite its superior RTD performance, a broader product CSD was obtained due to a high degree of supersaturation in MSMPR 2. This stresses the importance of controlling supersaturation to avoid excessive nucleation, as the occurrence of nucleation will result in a wider distribution of residence times, and hence widen the steady-state CSD. Since supersaturation is determined by operating temperature and mean residence time, independent manipulation of these process variables in each MSMPR stage can achieve the desired objective. For the α-GLY system in this study, an optimal operating strategy may be identified based on the dominant crystallization kinetics, whereby the

total mean residence time is distributed between each stage in a bid to increase crystal mean size and narrow CSD, without compromising thermodynamic yield (i.e. maintaining MSMPR 2 at 10 °C). A good approach would be to drive moderate nucleation in the first stage to obtain sufficient surface area/suspension density and eliminate fines in the second stage through longer residence times that favour crystal growth. Controlling crystallization mechanisms through decoupled operation is a key advantage of cascade design which has been demonstrated in several cascade optimization studies for systems with different crystallization kinetics.[54 – 57]

Lastly, to check for representative withdrawal in the 2-stage MSMPR crystallization, a steady-state sample was isolated via rapid intermittent withdrawal and compared with a sample withdrawn from the bottom of MSMPR 2. From Figure 21, it was concluded that both CSDs are comparable; however, it appears that a slightly greater number of coarse crystals are present at the bottom of MSMPR 2 than in the isolated sample.

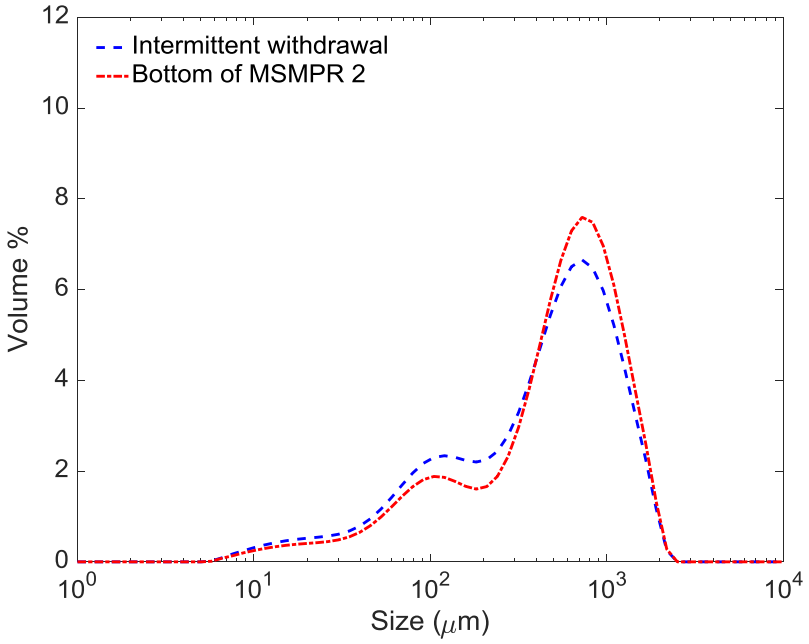

Figure 21 CSD comparison of steady-state samples taken by intermittent withdrawal and from the bottom of MSMPR 2.

This suggests that intermittent withdrawal may not be as efficient for suspensions containing coarse crystals. Other researchers[58] have observed similar behaviour using an intermittent pneumatic withdrawal method, whereby the mean particle size of the isolated sample was slightly smaller than in the crystallizer.

4. Conclusions

In this work, the continuous steady-state crystallization of α-GLY in a single- and 2-stage MSMPR crystallizer was made possible through the application of an intermittent vacuum-transfer technique. RTD characterisation confirmed previous simulation results by Su et al.[23] that material RTD in an MSMPR remains unchanged for different mean residence times. However, cooling crystallization experiments revealed the greater influence of secondary nucleation and growth mechanisms than RTD in determining steady-state product CSD. Specifically, secondary nucleation broadened steady-state CSD regardless of RTD performance; while growth-dominated processes improved product quality by narrowing CSD, increasing crystal mean size, and improving crystal shape. Operating at longer mean residence times was shown to be an effective approach for obtaining narrower steady-state CSDs, despite the characteristic broad RTD of the single-stage MSMPR.

Although the 2-stage MSMPR cascade achieved a better RTD and thermodynamic yield than feasible in the single-stage MSMPR system, a poorer product quality was obtained. This stresses that controlling supersaturation is key to improving CSD in an MSMPR cascade. CSD control is much easier in tubular crystallizers due to tighter control of supersaturation resulting from superior RTDs and heat transfer performance. To benefit from improved RTDs provided by multistage

MSMPR crystallizers, an optimum operating strategy must be identified that appropriately controls crystallization mechanisms in each MSMPR stage.

5. Acknowledgements

The authors would like to acknowledge access provided by the crystallization department housed within PT&D at AstraZeneca, Macclesfield.

6. Funding

This work was supported by the EPSRC (EP/I033459/1) Centre for Innovative Manufacturing in Continuous Manufacturing and Crystallization (CMAC) and the Doctoral Training Centre in Continuous Manufacturing and Crystallization (EP/K503289/1). All data created during this research are openly available from the Loughborough University data repository at https://doi.org/10.17028/rd.lboro.6429194.

7. Notes

The authors declare no competing financial interest.

8. Nomenclature

Abbreviations

API	active pharmaceutical ingredient
CLD	chord length distribution
COBC	continuous oscillatory baffled crystallizer
CSD	crystal size distribution

CQA	critical quality attribute
DFT	discrete Fourier transform
FBRM	focused beam reflectance measurement
FFT	fast Fourier transformation
GLY	glycine
MSMPR	mixed suspension mixed product removal
PFC	plug flow crystallizer
RCI	retreat curve impeller
RTD	residence time distribution
SAV	surface area to volume
SPC	smooth periodic constriction
SWMCL	square-weighted mean chord length

Symbols

A	heat transfer area (m^2)
C	dimensionless concentration for tracer (-)
c	tracer concentration ($g\ L^{-1}$)
c_i	initial tracer concentration ($g\ L^{-1}$)
C^*	equilibrium concentration at the specified operating temperature (g/g)
C_f	feed concentration to MSMPR 1 (g/g)
C_p	specific heat capacity the solution at the incoming feed temperature ($J\ kg^{-1}\ K^{-1}$)
C_{ss}^i	steady-state concentration in the ith MSMPR crystallizer (g/g)
D_{ax}	axial dispersion coefficient ($m^2\ s^{-1}$)

D_{ax}/uL	axial dispersion number (-)
D	impeller diameter (m)
d_p	diameter of spherical particles (m)
$d_{4,3}$	steady-state mean crystal size (μm)
g	acceleration due to gravity (m s^{-2})
h_i	process heat transfer coefficient (W m^{-2} K^{-1})
h_o	jacket heat transfer coefficient (W m^{-2} K^{-1})
h_w	wall heat transfer coefficient (W m^{-2} K^{-1})
k	upper size bin (-)
L	length of test section or distance between measurement points (m)
L_i	chord length in the ith size bin (μm)
N	impeller rotation speed (rps)
N_{Re}	impeller Reynolds number
N_{js}	just-suspended speed (rpm)
n	number of equal-sized tanks-in-series (-)
n_i	number of counts corresponding to the ith bin (-)
Re_o	oscillatory Reynolds number
S	impeller geometrical constant
T_{cr}	desired operating temperature (°C)
T_f	incoming feed temperature (°C)
T_j	MSMPR jacket temperature (°C)
t	time (s)
U	overall heat transfer coefficient (W m^{-2} K^{-1})

u	mean axial velocity (m s^{-1})
V_{cr}	crystallizer operating volume
X	mass ratio of solid to liquid (-)

Greek letters

ρ_l	liquid density (kg m^{-3})
ρ_p	particle density (kg m^{-3})
ρ_s	glycine solution density (kg m^{-3})
τ_L	mean residence time in the test section (s)
$\tau_{critical}$	critical mean residence time (min)
τ	mean residence time in the MSMPR crystallizer (min)
θ	dimensionless time (-)
μ	bulk fluid viscosity (Pa s)
ν	liquid kinematic viscosity (m^2 s)

9. References

1. Lawton, S.; Steele, G.; Shering, P. Continuous Crystallization of Pharmaceuticals Using a Continuous Oscillatory Baffled Crystallizer. *Org. Process Res. Dev.* **2009,** *13*, 1357 – 1363. https://doi.org/10.1021/op900237x.
2. Sang-Il Kwon, J.; Nayhouse, M.; Orkoulas, G.; Christofides, P.D. Crystal Shape and Size Control Using a Plug Flow Crystallization Configuration. *Chem. Eng. Sci.* **2014,** *119*, 30 – 39. https://doi.org/10.1016/j.ces.2014.07.058.
3. McWilliams, J. C.; Allian, A.D.; Opalka, S.M.; May, S.A.; Journet, M.; Braden, T.M. The Evolving State of Continuous Processing in Pharmaceutical API Manufacturing: A Survey of Pharmaceutical Companies

and Contract Manufacturing Organizations. *Org. Process Res. Dev.* **2018,** *22*, 1143 – 1166. https://doi.org/10.1021/acs.oprd.8b00160.

4. Schaber, S. D.; Gerogiorgis, D.I.; Ramachandra, R.; Evans, J.M.B.; Barton, P.I.; Trout, B.L. Economic Analysis of Integrated Continuous and Batch Pharmaceutical Manufacturing: A Case Study. *Ind. Eng. Chem. Res.* **2011,** *50*, 10083 – 10092. https://doi.org/10.1021/ie2006752.
5. Wang, J.; Li, F.; Lakerveld, R. Process Intensification for Pharmaceutical Crystallization. *Chem. Eng. Proc.* **2018,** *127*, 111 – 126. https://doi.org/10.1016/j.cep.2018.03.018.
6. Zhao, L.; Raval, V.; Briggs, N. E. B.; Bhardwaj, R. M.; McGlone, T.; Oswald, I. D. H.; Florence, A. J. From Discovery to Scale-Up: α-Lipoic Acid: Nicotinamide Co-Crystals in a Continuous Oscillatory Baffled Crystallizer. *Cryst. Eng. Comm.* **2014,** *16*, 5743 – 5934. https://doi.org/10.1039/C4CE00154K.
7. Agnew, L. R.; McGlone, T.; Wheatcroft, H.P.; Robertson, A.; Parsons, A.R.; Wilson, C.C. Continuous Crystallization of Paracetamol (Acetaminophen) Form II: Selective Access to a Metastable Solid Form. *Cryst. Growth Des*. **2017,** *17*, 2418 – 2427. https://doi.org/10.1021/acs.cgd.6b01831.
8. Srai, J. S.; Badman, C.; Krumme, M.; Futran, M.; Johnston, C. Future Supply Chains Enabled by Continuous Processing-Opportunities and Challenges May 20 – 21, 2014 Continuous Manufacturing Symposium. *Journal of Pharmaceutical Sciences* **2015,** *104*, 840 – 849. https://doi.org/10.1002/jps.24343.
9. Eder, R. J. P.; Radl, S.; Schmitt, E.; Innerhofer, S.; Maier, M.; Gruber-Woelfler, H.; Khinast, J.G. Continuously Seeded, Continuously Operated Tubular Crystallizer for the Production of Active Pharmaceutical Ingredients. *Cryst. Growth Des.* **2010,** *10*, 2247 – 2257. https://doi.org/10.1021/cg9015788.
10. Eder, R. J. P.; Schmitt, E.K.; Grill, J.; Radl, S.; Gruber-Woelfler, H.; Khinast, J.G. Seed Loading Effects on the Mean Crystal Size of Acetylsalicylic Acid in a Continuous-Flow Crystallization Device. *Cryst. Res. Technol.* **2011,** *46*, 227 – 237. https://doi.org/10.1002/crat.201000634.
11. Ferguson, S.; Morris, G.; Hao, H.; Barrett, M.; Glennon, B. In-Situ Monitoring and Characterization of Plug Flow Crystallizers. *Chem. Eng. Sci.* **2012,** *77*, 105 – 111. https://doi.org/10.1016/j.ces.2012.02.013.
12. Su, Q.; Benyahia, B.; Nagy, Z. K.; Rielly, C. D. Mathematical Modelling, Design, and Optimization of a Multi-Segment Multi-Addition Plug-Flow Crystallizer for Antisolvent Crystallizations. *Org. Process Res. Dev.* **2015,** *19*, 1859 – 1870. https://doi.org/10.1021/acs.oprd.5b00110.

13. McGlone, T.; Briggs, N.E.B.; Clark, C.A.; Brown, C.J.; Sefcik, J.; Florence, A.J. Oscillatory Flow Reactors (OFRs) for Continuous Manufacturing and Crystallization. *Org. Process Res. Dev.* **2015,** *19*, 1186–1202. https://doi.org/10.1021/acs.oprd.5b00225.

14. Ejim, L. N.; Yerdelen, S.; McGlone, T.; Onyemelukwe, I. I.; Johnston, B.; Florence, A. J.; Reis, N. M. A Factorial Approach to Understanding the Effect of Inner Geometry of Baffled Meso-Scale Tubes on Solids Suspension and Axial Dispersion in Continuous, Oscillatory Liquid-Solid Plug Flows. *Chem. Eng. J.* **2017,** *308*, 669 – 682. https://doi.org/10.1016/j.cej.2016.09.013.

15. Randolph, A.; Larson, M. *Theory of particulate processes: Analysis and Techniques of Continuous Crystallization;* Academic Press: New York, 1971. https://doi.org/10.1016/B978-0-12-579650-7.X5001-5.

16. Ferguson, S.; Morris, G.; Hao, H.; Barret, M.; Glennon, B. Characterization of the Anti-Solvent Batch, Plug Flow and MSMPR Crystallization of Benzoic Acid. *Chem. Eng. Sci.* **2013,** *104*, 44 – 54. https://doi.org/10.1016/j.ces.2013.09.006.

17. Brown, C. J.; McGlone, T.; Yerdelen, S.; Srirambhatla, V.; Mabbot, F.; Gurung, R.; Briuglia, M.L.; Ahmed, B.; Polyzois, H.; McGinty, J.; Perciballi, F.; Fysikopoulos, D.; MacFhionnghaile, P.; Siddique, H.; Raval, V.; Harrington, T.S.; Vassileiou, A.D.; Robertson, M.; Prasad, E.; Johnston, A.; Johnston, B.; Nordon, A.; Srai, J.S.; Halbert, G.; ter Horst, J.H.; Price, C.J.; Rielly, C.D.; Sefcik, J.; Florence, A.J. Enabling Precision Manufacturing of Active Pharmaceutical Ingredients: Workflow for Seeded Cooling Continuous Crystallizations. *Mol. Syst. Des. Eng.* **2018,** *3*, 518 – 549. https://doi.org/10.1039/C7ME00096K.

18. Porru, M.; Özkan, L. Control of a Two-Stage Mixed Suspension Mixed Product Removal Crystallizer. *IFAC PapersOnLine*, **2018,** *51-18*, 898 – 903. https://doi.org/10.1016/j/ifacol.2018.09.231.

19. Yang, Y.; Nagy, Z.K. Model-Based Systematic Design and Analysis Approach for Unseeded Combined Cooling and Antisolvent Crystallization (CCAC) Systems. *Cryst. Growth Des.* **2014,** *14*, 687 – 698. https://doi.org/10.1021/cg401562t.

20. Briggs, N. E. B.; Schacht, U.; Raval, V.; McGlone, T.; Sefcik, J.; Florence, A.J. Seeded Crystallization of β-L-Glutamic Acid in a Continuous Oscillatory Baffled Crystallizer. *Org. Process Res. Dev.* **2015,** *19*, 1903 – 1911. https://doi.org/10.1021/acs.oprd.5b00206.

21. Siddique, H.; Brown, C.J.; Houson, I.; Florence, A.J. Establishment of a Continuous Sonocrystallization Process for Lactose in an Oscillatory Baffled Crystallizer. *Org. Process Res. Dev.* **2015,** *19*, 1871 – 1881. https://doi.org/10.1021/acs.oprd.5b00127.

22. Hou, G.; Power, G.; Barrett, M.; Glennon, B. Morris, G.; Zhao, Y. Development and Characterization of a Single Stage Mixed-Suspension, Mixed-Product-Removal Crystallization Process with a Novel Transfer Unit. *Cryst. Growth Des.* **2014,** *14*, 1782 – 1793. https://doi.org/10.1021/cg401904a.

23. Su, Q.; Rielly, C.D.; Powell, K.A.; Nagy, Z.K. Mathematical Modelling and Experimental Validation of a Novel Periodic Flow Crystallization Using MSMPR Crystallizers. *AIChE J.* **2017,** *63*, 1313 – 1327. https://doi.org/10.1002/aic.15510.

24. Garside, J.; Mersmann, A.; Nyvlt, J. *Measurement of Crystal Growth and Nucleation Rates*. 2nd ed.; Institution of Chemical Engineers: Rugby, U.K., 2002.

25. Griffin, D. W.; Mellichamp, D. A.; Doherty, M. F. Reducing the Mean Size of API Crystals by Continuous Manufacturing with Product Classification and Recycle. *Chem. Eng. Sci.* **2010,** *65*, 5770 – 5780. https://doi.org/10.1016/j.ces.2010.05.026.

26. Yang, Y.; Song, L.; Gao, T.; Nagy, Z. K. Integrated Upstream and Downstream Application of Wet Milling with Continuous Mixed Suspension Mixed Product Removal Crystallization. *Cryst. Growth Des.* **2015,** *15*, 5879 – 5885. https://doi.org/10.1021/acs.cgd.5b01290.

27. Acevedo, D.; Kamaraju, V.K.; Glennon, B.; Nagy, Z.K. Modeling and Characterization of an in Situ Wet Mill Operation. *Org. Process Res. Dev.* **2018,** *21*, 1069 – 1079. https://doi.org/10.1021/acs.oprd.7b00192.

28. Gao, Z.; Wu, Y.; Gong, J.; Wang, J.; Rohani, S. Continuous Crystallization of α-Form L-Glutamic Acid in an MSMPR-Tubular Crystallizer System. *J. Cryst. Growth* **2018.** https://doi.org/10.1016/j.jcrysgro.2018.07.007**.**

29. Randolph, A.D.; Deepak, C.; Iskander, M. On the Narrowing of Particle-Size Distributions in Staged Vessels with Classified Product Removal. *AIChE J.* **1968,** *14*, 827 – 830. https://doi.org/10.1002/aic.690140532.

30. Tavare, N.; Garside, J.; Larson, M. Crystal Size Distribution from a Cascade of MSMPR Crystallizers with Magma Recycle. *Chem. Eng. Commun.* **1986,** *47*, 185 – 199. https://doi.org/10.1080/00986448608911763.

31. Zhang, H.; Quon, J.; Alvarez, A.J.; Evans, J.; Myerson, A.S.; Trout, B. Development of Continuous Anti-Solvent/Cooling Crystallization Process Using Cascaded Mixed Suspension, Mixed Product Removal Crystallizers. *Org. Process Res. Dev.* **2012,** *16*, 915 – 924. https://doi.org/10.1021/op2002886.
32. Quon, J. L.; Zhang, H.; Alvarez, A.; Evans, J; Myerson, A.S.; Trout, B.L. Continuous Crystallization of Aliskiren Hemifumarate. *Cryst. Growth Des.* **2012,** *12*, 3036 – 3044. https://doi.org/10.1021/cg300253a.
33. Morris, G.; Power, G.; Ferguson, S.; Barrett, M.; Hou, G.; Glennon, B. Estimation of Nucleation and Growth Kinetics of Benzoic Acid by Population Balance Modelling of a Continuous Cooling Mixed Suspension, Mixed Product Removal Crystallizer. *Org. Process Res. Dev.* **2015,** *19*, 1891 – 1902. https://doi.org/10.1021/acs.oprd.5b00139.
34. Agimelen, O. S.; Hamilton, P.; Haley, I.; Nordon, A.; Vasile, M.; Sefcik, J.; Mulholland, A.J. Estimation of Particle Size Distribution and Aspect Ratio of Non-Spherical Particles from Chord Length Distribution. *Chem. Eng. Sci.* **2015,** *123*, 629 – 640. https://doi.org/10.1016/j.ces.2014.11.014.
35. Zheng, M.; Mackley, M. The Axial Dispersion Performance of an Oscillatory Flow Meso-Reactor with Relevance to Continuous Flow Operation. *Chem. Eng. Sci.* **2008,** *63*, 1788 – 1799. https://doi.org/10.1016/j.ces.2007.12.020.
36. Bischoff, K.N.; Levenspiel, O. Fluid Dispersion-Generalization and Comparison of Mathematical Models – I. Generalization of Models. *Chem. Eng. Sci.* **1962,** *17*, 245 – 255. https://doi.org/10.1016/0009-2509(62)85003-9.
37. Levenspiel, O. *Chemical Reaction Engineering*. 3rd ed.; John Wiley & Sons: London, 1999.
38. Levenspiel, O.; Smith, W.K. Notes on the Diffusion-Type for the Longitudinal Mixing of Fluids in Flow. *Chem. Eng. Sci.* **1957,** *6*, 227 – 233. https://doi.org/10.1016/0009-2509(96)81817-3.
39. Fogler, H. S. *Elements of Chemical Reaction Engineering*. 3rd ed.; Prentice Hall: Upper Saddle River, NJ, 1999.
40. Verlaan, P.; Van Eijs, A.M.M.; Tramper, J.; Van't Riet, K.; Luyben, K. Estimation of Axial Dispersion in Individual Sections of an Airlift-Loop Reactor. *Chem. Eng. Sci.* **1989,** *44*, 1139 – 1146. https://doi.org/10.1016/0009-2509(89)87013-7.
41. Obradovic, B.; Dudukovic, A.; Vunjak-Novakovic, G. Response Data Analysis of a Three Phase Airlift Reactor. *Trans IChemE* **1997,** *75*, Part A, 473 – 479. https://doi.org/10.1205/026387697523976.

42. Zwietering, T. N. Suspending of Solid Particles in Liquid by Agitators. *Chem. Eng. Sci.* **1958,** *8*, 244 – 253. https://doi.org/10.1016/0009-2509(58)85031-9.

43. Ayranci, I.; Kresta, S. M. Design Rules for Suspending Concentrated Mixtures of Solids in Stirred Tanks. *Chem. Eng. Res. Des.* **2011,** *89*, 1961 – 1971. https://doi.org/10.1016/j.cherd.2011.01.008.

44. Wadnerkar, D.; Utikar, R.P.; Tade, M.O.; Pareek, V.K. CFD Simulation of Solid-Liquid Stirred Tanks. *Advanced Powder Technology* **2012,** *23*, 445 – 453. https://doi.org/10.1016/j.apt.2012.03.007.

45. Kneule, F. Die Prüfung von Rührern durch Löslichkeitsbestimmung. *Chemie Ingenieur Technik* **1956,** *28*, 221 – 225. https://doi.org/10.1002/cite.330280316.

46. Nienow, A.W.; Edwards, M.F.; Harnby, N. *Mixing in the Process Industries*. 2nd ed.; Butterworth-Heinemann, 1997. https://doi.org/10.1016/B978-0-7506-3760-2.X5020-3.

47. Nienow, A.W. The Mixer as a Reactor: Liquid/solid Systems. In *Mixing in the Process Industries;* Nienow, A.W., Edwards, M.F., Harnby, N., Eds.; 2nd ed.; Butterworth-Heinemann, 1997; 349 – 411, https://doi.org/10.1016/B978-0-7506-3760-2.X5020-3.

48. Rielly, C. D.; Habib, M.; Sherlock, J. P. Flow and Mixing Characteristics of a Retreat Curve Impeller in a Conical-Based Vessel. *Chem. Eng. Res. Des.* **2007,** *85*, 953 – 962. https://doi.org/10.1205/cherd07002.

49. Ayranci, I.; Kresta, S. M. Critical Analysis of Zwietering Correlation for Solids Suspension in Stirred Tanks. *Chem. Eng. Res. Des.* **2014,** *92*, 413 – 422. https://doi.org/10.1016/j.cherd.2013.09.005.

50. Blais, B.; Bertrand, O.; Fradette, L.; Bertrand, F. CFD-DEM Simulations of Early Turbulent Solid–Liquid Mixing: Prediction of Suspension Curve and Just-Suspended Speed. *Chem. Eng. Res. Des.* **2017,** *123*, 388 – 406. https://doi.org/10.1016/j.cherd.2017.05.021.

51. Choi, B. S.; Wan, B.; Philyaw, S.; Dhanasekharan, K.; Ring, T.A. Residence Time Distributions in a Stirred Tank: Comparison of CFD Predictions with Experiment. *Ind. Eng. Chem. Res.* **2004,** *43*, 6548 – 6556. https://doi.org/10.1021/ie0308240.

52. Patwardhan, A. W. Prediction of Residence Time Distribution of Stirred Reactors. *Industrial and Engineering Chemistry Research* **2001,** *40*, 5686 – 5695. https://doi.org/10.1021/ie0103198.

53. Onyemelukwe, I.I.; Benyahia, B.; Reis, N.M.; Nagy, Z.K.; Rielly, C.D. The Heat Transfer Characteristics of a Mesoscale Continuous Oscillatory Flow Crystallizer with Smooth Periodic Constrictions. *Int. J. Heat Mass Transfer* **2018,** *123*, 1109 – 1119. https://doi.org/10.1016/j.ijheatmasstransfer.2018.03.015.

54. Power, G.; Hou, G.; Kamaraju, V. K.; Morris, G.; Zhao, Y.; Glennon, B. Design and Optimization of a Multistage Continuous Cooling Mixed Suspension, Mixed Product Removal Crystallizer. *Chem. Eng. Sci.* **2015,** *133*, 125 – 139. https://doi.org/10.1016/j.ces.2015.02.014.

55. Vetter, T.; Burcham, C. L.; Doherty, M. F. Regions of Attainable Particle Sizes in Continuous and Batch Crystallization Processes. *Chem. Eng. Sci.* **2014,** *106*, 167–180. https://doi.org/10.1016/j.ces.2013.11.008.

56. Vetter, T.; Burcham, C. L; Doherty, M. F. Designing Robust Crystallization Processes in the Presence of Parameter Uncertainty Using Attainable Regions. *Ind. Eng. Chem. Res.* **2015,** *54*, 10350 – 10363. https://doi.org/10.1021/acs.iecr.5b00693.

57. Park, K.; Kim, D. Y.; Yang, D. R. Operating Strategy for Continuous Multistage Mixed Suspension and Mixed Product Removal (MSMPR) Crystallization Processes Depending on Crystallization Kinetic Parameters. *Ind. Eng. Chem. Res.* **2016,** *55*, 7142 – 7153. https://doi.org/10.1021/acs.iecr.6b01386.

58. Yang, X.; Acevedo, D.; Mohammad, A.; Pavurala, N.; Wu, H.; Brayton, A.L.; Shaw, R.A.; Goldman, M.J.; He, F.; Li, S.; Fisher, R.J.; O'Connor, T.F.; Cruz, C.N. Risk Considerations on Developing a Continuous Crystallization System for Carbamazepine. *Org. Process Res. Dev.* **2017,** *21*, 1021 – 1033. https://doi.org/10.1021/acs.oprd.7b00130.

For Table of Contents Use Only

The role of residence time distribution in the continuous steady-state MSMPR crystallization of glycine

Iyke I. Onyemelukwe[a,*], Anna R. Parsons[c], Helen P. Wheatcroft[c], Amy Robertson[c], Zoltan K. Nagy[a,b], Chris D. Rielly[a,*]

[a]*EPSRC Centre for Innovative Manufacturing in Continuous Manufacturing and Crystallization, c/o Department of Chemical Engineering, Loughborough University, Loughborough, Leicestershire, LE11 3TU, UK*
[b]*School of Chemical Engineering, Purdue University, West Lafayette, IN 47907, USA*
[c]*PT&D, AstraZeneca Macclesfield, Silk Road Business Park, Charter Way, Hurdsfield Industrial Estate, Macclesfield, SK10 2NA, UK*

We report the steady-state cooling crystallization of α-glycine in a single- and 2-stage MSMPR crystallizer. Using the residence time distribution analysis and process analytical technology, we demonstrate the need for optimum control of supersaturation to benefit from improved residence time distributions provided by multistage MSMPR crystallizers.